DTU Library

Conservation laws for interacting magnetic nanoparticles at finite temperature

Durhuus, Frederik L.; Beleggia, Marco; Frandsen, Cathrine

Link back to DTU Orbit

Conservation laws for interacting magnetic nanoparticles at finite temperature

Frederik L. Durhuus [1], Marco Beleggia [2,3] and Cathrine Frandsen [1,*]

[1]*Department of Physics, Technical University of Denmark, 2800 Kgs. Lyngby, Denmark*
[2]*Department of Physics, University of Modena and Reggio Emilia, 41125 Modena, Italy*
[3]*DTU Nanolab, Technical University of Denmark, 2800 Kgs. Lyngby, Denmark*

We establish a general Langevin dynamics model of interacting, single-domain magnetic nanoparticles (MNPs) in liquid suspension at finite temperature. The model couples the Landau-Lifshitz-Gilbert equation for the moment dynamics with the mechanical rotation and translation of the particles. Within this model, we derive expressions for the instantaneous transfer of energy, linear, and angular momentum between the particles and with the environment. We demonstrate by numerical tests that all conserved quantities are fully accounted for, thus validating the model and the transfer expressions. The energy transfer expressions derived here are also useful analysis tools to decompose the instantaneous, nonequilibrium power loss at each MNP into different loss channels. To demonstrate the model capabilities, we analyze simulations of MNP collisions and high-frequency hysteresis in terms of power and energy contributions.

I. INTRODUCTION

Magnetic nanoparticles (MNPs) are currently under intense study for a broad range of applications including inductive components for power electronics [1], heating catalytic reactions [2,3], drug delivery [4], hyperthermia treatment of cancer [5–7], and various biosensor techniques [8] such as magnetic particle imaging [9].

Central to these technologies is the response of MNPs to applied, magnetic fields, in particular their hysteresis loops and resulting heat dissipation. Analytical models for the magnetic response of an MNP ensemble do exist [10,11], but they generally assume spatial homogeneity, linear response, and quasiequilibrium. However, recent studies have highlighted the importance of the local temperature profile [12], MNP interactions [13–16], nonequilibrium dynamics [17], and aggregation [18,19] in addition to coupling between magnetic and mechanical degrees of freedom [20,21].

One of the most advanced and versatile methods for modeling MNPs is Langevin dynamics [22], which incorporates all of the aforementioned complexities. Here the equations of motion are derived from the total system energy, with the inclusion of stochastic and damping terms to model thermal noise and dissipation, respectively. Some studies have treated special cases or linearized versions of the equations analytically [23–27], but usually in their full nonlinear form they are solved numerically. The most common method is direct time-step integration [28,29] also known as a Langevin dynamics (LD) simulation, which we use in this paper. The main alternative is kinetic Monte Carlo methods [30,31].

LD simulation studies include aggregation dynamics in zero field [32–35], uniform [36,37], and gradient fields [38],

as well as magnetic susceptibility computations [39–41] and numerous simulations of hysteresis heating in alternating fields, both in liquid suspension [34,42–47] and fixed in space [13,16,30,48,49].

The standard way to implement Langevin dynamics of MNPs is to assume a single magnetic moment $\boldsymbol{\mu}$, described by the Landau-Lifshitz-Gilbert (LLG) equation [50]. The system energy depends on the moment orientation relative to the underlying atomic lattice, hence, the LLG is coupled to the mechanical rotation of the particle. Recently, several authors [25,43,51,52] derived a more complete model of this magnetomechanical coupling, which includes the intrinsic spin and orbital angular momentum of electrons $\mathbf{S} = -\boldsymbol{\mu}/\gamma$, however, only for the single-MNP case. Unlike previous work, e.g., [39,42,47], this new model obeys conservation of total angular momentum $\mathbf{J}$. It has subsequently been studied both numerically [43,44] and analytically [24,51].

As stated by Usov and Liubimov [52], $\mathbf{J}$ conservation is only important in low-friction cases, such as nanomagnets suspended in vacuum. Nevertheless, conservation laws serve as an important test of theoretical arguments in all cases, leading to a more solid foundation upon which to impose approximations. Also, there are examples of current [53] and proposed [51,54] experiments where $\mathbf{J}$ conservation plays a starring role.

Another recent branch of inquiry is the effect of temperature on energy transfer. By the fluctuation-dissipation theorem [55], each dissipation channel has corresponding thermal fluctuations, which lead to a mutual energy exchange between particles and environment. These thermal power contributions must be derived explicitly to understand the instantaneous energy transfer at the nanoscale [14,49], which is essential to predict the local temperature distribution.

In this paper we derive a generalization of the $\mathbf{J}$-conserving model to systems of multiple MNPs at finite temperature

---

with dipole-dipole interactions. This leads to additional subtleties in accounting for energy and angular momentum, so we present a detailed analysis of the transfer of conserved quantities that includes analytical and numerical demonstrations of conservation up to entirely physical exchange with the environment.

This paper may be regarded as a generalization of the work by Helbig *et al.* [45] to multiple MNPs at finite temperature, and of the work of Leliaert *et al.* [49] to include mechanical motion.

A common simplification is the rigid dipole approximation (RDA), where $\boldsymbol{\mu}$ is assumed locked relative to the particle's atomic lattice, effectively removing the LLG part of the model. This circumvents the moment dynamics, which are generally several orders of magnitude faster than mechanical rotation [39], thus permitting far longer time steps. Another simplification is the overdamped limit, where inertia is neglected, as friction usually dominates for nanoparticles and microparticles in liquid [56]. The RDA and the overdamped limit as well as the micromagnetics of immobilized particles can all be derived as limiting cases of our model.

Aside from model validation, the presented transfer formulas are useful analysis tools. Typically, energy dissipation is determined by the area of a hysteresis curve, however, this is only possible for the average dissipation rate of periodically driven systems in steady state. From the formulas presented in the paper, one can calculate the instantaneous power dissipation at each MNP and decompose into different loss channels. In particular, magnetic losses from Gilbert damping heat the MNP itself, while mechanical losses from viscous damping heat the surrounding fluid. This gives a detailed, local perspective, applicable to nonequilibrium dynamics, which we demonstrate by analyzing example simulations with and without an external, alternating magnetic field. We note that viscous losses correspond to Brownian relaxation where the whole particle is rotating, while magnetic losses correspond to Néel relaxation, where only the magnetic moment is rotating.

The paper is structured as follows. In Sec. II we systematically derive a Langevin dynamics model for MNPs in fluid suspension, which has vacuum and solid suspension as limiting cases. In Sec. III we formally derive expressions for the transfer of conserved quantities and discuss their application. In Sec. IV we discuss common model approximations in the context of conservation laws and the many characteristic frequencies of these systems. In Sec. V we present numerical validation of the conservation laws at finite temperature and example simulations of 1, 2, and 10 particle systems at zero temperature. Video animations of the simulations are shown in the Supplemental Material [57]. Finally, in Sec. VI we discuss possible model generalizations, with supporting calculations shown in the Supplemental Material [57].

II. MODEL

We consider a collection of identical, ferromagnetic, or ferrimagnetic, spherical MNPs. Let $\boldsymbol{\mu}_i$ be the net magnetic moment of the ith MNP, R radius, V volume, $\mathbf{r}_i$ the position of its center and $\mathbf{v}_i = \dot{\mathbf{r}}_i$ its velocity. We assume internal exchange coupling is strong enough to ensure uniform magnetization of constant magnitude M, hence, $\boldsymbol{\mu}_i = \mu \mathbf{m}_i$ where $\mathbf{m}_i$
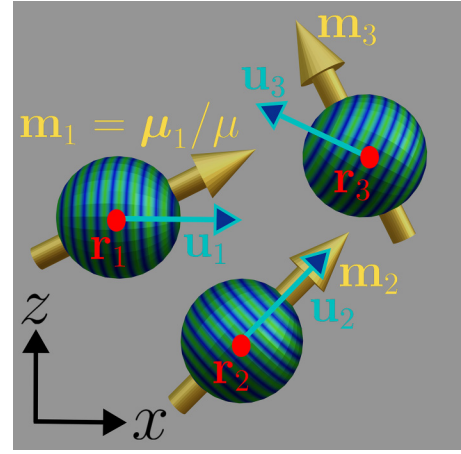

FIG. 1. Illustration of system with three magnetic nanoparticles (MNPs). MNPs (spheres) and magnetic moments (yellow 3D vectors) are drawn in Blender [58] with the same code used to visualize simulations in Figs. 4 and 5, and the supplemental videos [57]. The center positions $\mathbf{r}_i$, normalized moments $\mathbf{m}_i = \boldsymbol{\mu}_i/MV$ and orientation vectors $\mathbf{u}_i$ are indicated. The anisotropy axes are perpendicular to the blue and green circles and parallel to $\mathbf{u}_i$, so the anisotropy energy is lowest when $\mathbf{u}_i \parallel \mathbf{m}_i$ which is the case for particle 2.

is a unit vector and $\mu = VM$ is constant. We specify particle orientation by the unit vector $\mathbf{u}_i$ which is fixed along the chosen anisotropy axis (defined in Sec. II A 2), so $\mathbf{u}$ follows the mechanical rotation. See Fig. 1 for an illustration. Finally, let $\boldsymbol{\omega}_i$ denote angular velocity, in the sense that MNP i rotates ω_i radians per second counterclockwise around the vector $\boldsymbol{\omega}_i$. This is the model system we analyze in Secs. II–V, and we discuss possible generalizations in Sec. VI.

A. Magnetic interactions

1. Magnetic fields

The magnetic interactions of uniformly magnetized spheres are (up to relativistic corrections) precisely those of point dipoles located at their centers [59]. That is, each MNP produces a dipole field outside its surface, and the interaction energy between MNP i and j is $E_{ij}^{\text{int}} = -\boldsymbol{\mu}_i \cdot \mathbf{B}_{ji}^{\text{dip}}$ where $\mathbf{B}_{ji}^{\text{dip}}$ is the field from MNP j evaluated at $\mathbf{r}_i$.

The total dipole interaction energy is then

$$E^{\text{int}} = \frac{1}{2} \sum_i \sum_{j \neq i} E_{ij}^{\text{int}} = -\frac{1}{2} \sum_i \boldsymbol{\mu}_i \cdot \mathbf{B}_i^{\text{dip}}$$

with a factor of $\frac{1}{2}$ to avoid double counting. $\mathbf{B}_i^{\text{dip}}$ is the field on the ith MNP from all the rest, which is given by [60]

$$\mathbf{B}_i^{\text{dip}} = \frac{\mu_0}{4\pi} \sum_{j \neq i} \frac{1}{r_{ji}^3} [3(\boldsymbol{\mu}_j \cdot \hat{\mathbf{r}}_{ji})\hat{\mathbf{r}}_{ji} - \boldsymbol{\mu}_j], \quad (1)$$

where

$$\mathbf{r}_{ji} = \mathbf{r}_i - \mathbf{r}_j, \quad r_{ji} = |\mathbf{r}_{ji}|, \quad \hat{\mathbf{r}}_{ji} = \mathbf{r}_{ji}/r_{ji}.$$

We also consider a uniform, but time-varying, field $\mathbf{B}^{\text{ext}}$ generated by external currents, which gives the

Zeeman energy [61]

$$E_i^{\text{Zee}} = -\boldsymbol{\mu}_i \cdot \mathbf{B}^{\text{ext}}. \tag{2}$$

2. Uniaxial anisotropy

There are a number of energy terms which give the magnetization a preferred direction relative to the particle's crystal lattice, namely, shape, magnetocrystalline, surface, and strain anisotropy [62]. The latter two primarily induce nonuniform magnetization, which we neglect entirely, and shape anisotropy is absent for a sphere.

Magnetocrystalline anisotropy results from relativistic spin-orbit and spin-spin coupling, which to lowest order yields [63] $E_{\text{MC}} = \frac{1}{2}V\mathbf{m}^T K\mathbf{m}$, where K is a rank-2 tensor. Because this is a relativistic perturbation, we expect higher-order terms to be substantially smaller. We can always pick a local coordinate system such that K is diagonal. We call the corresponding eigenvalues K_x, K_y, K_z. Then, using $m_z^2 = 1 - m_x^2 - m_y^2$,

$$\frac{1}{V}E_{\text{MC}} = \frac{1}{2}\mathbf{m}^T K\mathbf{m}$$
$$= \text{const} + \frac{1}{2}(K_x - K_z)m_x^2 + \frac{1}{2}(K_y - K_z)m_y^2.$$

If K_x, K_y, K_z are all different, then this defines a hard, easy, and intermediate axis, i.e., triaxial anisotropy.

Typically, in MNP studies, it is implicitly assumed that there is rotation symmetry about an axis $\mathbf{u}$, so that two of the eigenvalues are equal. For instance, if $\mathbf{u} = \mathbf{e}_x$ then $K_x = K_\parallel$ and $K_y = K_z = K_\perp$. The energy may then be written in the coordinate independent form

$$E_{\text{MC}} = \text{const} - KV(\mathbf{m} \cdot \mathbf{u})^2, \tag{3}$$

where $K = \frac{1}{2}(K_\parallel - K_\perp)$. Evidently Eq. (3) describes uniaxial anisotropy, with either a hard axis $(K < 0)$ or an easy axis $(K > 0)$.

We refer to the literature for higher-order anisotropy terms with lower symmetry [62,64,65].

B. Conserved quantities

1. Momenta

The total angular momentum of MNP i in its own rest frame is

$$\mathbf{J}_i = \mathbf{L}_i + \mathbf{S}_i, \ \mathbf{L}_i = I\boldsymbol{\omega}_i, \ \mathbf{S}_i = -\gamma^{-1}\boldsymbol{\mu}_i, \tag{4}$$

where I is the moment of inertia, γ is the gyromagnetic ratio, $\mathbf{L}_i$ is the mechanical angular momentum, and $\mathbf{S}_i$ is the angular momentum associated with the magnetic moment. $\mathbf{S}_i$ comprises electron spin and orbital angular momentum [66].

The angular momentum of the whole MNP system is

$$\mathbf{J} = \mathbf{L} + \mathbf{S},$$
$$\mathbf{L} = \sum_i (\mathbf{L}_i + \mathbf{r}_i \times \mathbf{p}_i), \ \mathbf{S} = \sum_i \mathbf{S}_i, \tag{5}$$

where $\mathbf{p}_i$ is the linear momentum. Aside from the sum of *intrinsic* angular momenta $\mathbf{J}_i$, there is an *extrinsic* mechanical contribution from motion relative to the rest of the system, i.e., $\sum_i \mathbf{r}_i \times \mathbf{p}_i$.

The system linear momentum is all mechanical and given simply by

$$\mathbf{p} = \sum_i \mathbf{p}_i. \tag{6}$$

We discuss the transfer of linear and angular momenta in Sec. III, in particular proving that the model obeys physical conservation laws.

2. Energy

The system energy is, up to a constant,

$$E = \frac{1}{2}I\sum_i \omega_i^2 + \frac{1}{2}\mathfrak{m}\sum_i v_i^2 - \frac{1}{2}\sum_i \boldsymbol{\mu}_i \cdot \mathbf{B}_i^{\text{dip}}$$
$$- \sum_i \boldsymbol{\mu}_i \cdot \mathbf{B}^{\text{ext}} - KV\sum_i (\mathbf{m}_i \cdot \mathbf{u}_i)^2, \tag{7}$$

where $\mathfrak{m}$ is the mass of each particle. The first two terms are rotational and translational kinetic energy, while the last three are explained in Secs. II A 1 and II A 2.

C. Energy-conserving equations of motion

The torque $\boldsymbol{\tau}$ on a rigid body is defined as the energy gain under an infinitesimal rotation $\delta\boldsymbol{\phi}$. That is, when $\mathbf{u} \to \mathbf{u} + \delta\boldsymbol{\phi} \times \mathbf{u}$ we have by definition

$$\Delta E[\delta\boldsymbol{\phi}] = -\boldsymbol{\tau} \cdot \delta\boldsymbol{\phi} + O(\delta\phi^2).$$

To first order in $\delta\phi$,

$$E[\mathbf{u} + \delta\boldsymbol{\phi} \times \mathbf{u}] - E[\mathbf{u}] = \frac{\partial E}{\partial \mathbf{u}} \cdot (\delta\boldsymbol{\phi} \times \mathbf{u})$$
$$= \left(\mathbf{u} \times \frac{\partial E}{\partial \mathbf{u}}\right) \cdot \delta\boldsymbol{\phi},$$

thus, the time derivative of $\mathbf{L}_i$ is

$$\dot{\mathbf{L}}_i = \boldsymbol{\tau}_i = \frac{\partial E}{\partial \mathbf{u}_i} \times \mathbf{u}_i. \tag{8}$$

Similarly [25], $\dot{\mathbf{S}}_i = \partial_{\mathbf{m}_i} E \times \mathbf{m}_i$ for the variation of magnetic angular momentum, and from an infinitesimal displacement, one finds $\dot{\mathbf{p}}_i = -\partial_{\mathbf{r}_i} E$ for the variation of linear momentum.

It then follows from Eqs. (4) and (7) after some algebra that

$$\dot{\mathbf{m}}_i = -\gamma\mathbf{m}_i \times \left(\mathbf{B}_i^{\text{dip}} + \mathbf{B}_i^{\text{ext}} + \mathbf{B}_i^{\text{ani}}\right), \tag{9}$$

$$I\dot{\boldsymbol{\omega}}_i = -\mu_i\mathbf{m}_i \times \mathbf{B}_i^{\text{ani}}, \tag{10}$$

$$\mathfrak{m}\dot{\mathbf{v}}_i = \mathbf{F}_i^{\text{dip}}, \tag{11}$$

where

$$\mathbf{B}_i^{\text{ani}} = 2\frac{K_i}{M_i}(\mathbf{m}_i \cdot \mathbf{u}_i)\mathbf{u}_i \tag{12}$$

is an effective field from uniaxial anisotropy and

$$\mathbf{F}_i^{\text{dip}} = \frac{3\mu_0}{4\pi}\sum_{j\neq i}\frac{1}{r_{ji}^4}[(\boldsymbol{\mu}_i \cdot \hat{\mathbf{r}}_{ji})\boldsymbol{\mu}_j + (\boldsymbol{\mu}_j \cdot \hat{\mathbf{r}}_{ji})\boldsymbol{\mu}_i$$
$$+ (\boldsymbol{\mu}_i \cdot \boldsymbol{\mu}_j)\hat{\mathbf{r}}_{ji} - 5(\boldsymbol{\mu}_i \cdot \hat{\mathbf{r}}_{ji})(\boldsymbol{\mu}_j \cdot \hat{\mathbf{r}}_{ji})\hat{\mathbf{r}}_{ji}]. \tag{13}$$

When differentiating the dipole-dipole interaction, note that $\mathbf{B}_j^{\text{dip}}$ contains $\boldsymbol{\mu}_i$. We observe that the forces in Eq. (13),

and the torques $\boldsymbol{\mu}_i \times \mathbf{B}_i^{\text{dip}}$, are precisely those between point dipoles [67].

Equations (9) to (11) constitute a molecular dynamics model, which amounts to zero-temperature dynamics in vacuum. In Langevin dynamics, there are also fluctuation and dissipation terms to describe coupling with the environment, i.e., all the degrees of freedom that are not modeled explicitly.

D. Fluctuations and dissipation

1. Gilbert damping

To model dissipative coupling between magnetic moments and internal degrees of freedom, such as electrons and phonons, we use the phenomenological Gilbert damping torque [50], which converts magnetic angular momentum to mechanical:

$$\dot{\mathbf{S}}_i = \dot{\mathbf{S}}_i\big|_{\alpha=0} + \boldsymbol{\tau}_i^\alpha \quad \text{and} \quad \dot{\mathbf{L}}_i = \dot{\mathbf{L}}_i\big|_{\alpha=0} - \boldsymbol{\tau}_i^\alpha, \qquad (14)$$

where at zero temperature

$$\boldsymbol{\tau}_i^\alpha\big|_{T=0} = -\alpha\mu\gamma^{-1}[\mathbf{m}_i \times \dot{\mathbf{m}}_i + \mathbf{m}_i \times (\mathbf{m}_i \times \boldsymbol{\omega}_i)], \qquad (15)$$

and α is the material-specific Gilbert damping constant. See Sec. II D 3 for the effect of temperature.

The first term is the standard Gilbert torque in the rest frame of the particle, and the second an additional torque from transforming to the laboratory frame [25,43], which has been argued to produce the Barnett effect (change in magnetization from mechanical rotation) [25,68]. Indeed, the second term is proportional to the Barnett field [25,54]

$$\mathbf{B}_i^{\text{Bar}} = -\gamma^{-1}\boldsymbol{\omega}_i. \qquad (16)$$

2. Viscous damping

Often MNPs are studied in fluid suspension, in which case there is viscous damping from MNPs colliding with the fluid particles, e.g., water molecules. For an isolated sphere at low Reynolds number (Stokes flow regime) in a stationary fluid, the exact expressions for the damping force and torque are [69]

$$\mathbf{F}^{\text{visc}} = -\zeta^{\text{t}}\mathbf{v}, \quad \boldsymbol{\tau}^{\text{visc}} = -\zeta^{\text{r}}\boldsymbol{\omega},$$

where

$$\zeta^{\text{t}} = 6\pi\eta R, \quad \zeta^{\text{r}} = 8\pi\eta R^3 \qquad (17)$$

are the translational and rotational friction coefficients and η is dynamic viscosity. We neglect hydrodynamic interactions between the MNPs (see Sec. VI for discussion and references).

3. Fluctuations

By the fluctuation-dissipation theorem [55], for each dissipation mechanism there are corresponding thermal fluctuations. For the viscous damping, random collisions between fluid particles and MNPs lead to Brownian motion, described by a thermal force $\mathbf{F}^{\text{th}}$ and torque $\boldsymbol{\tau}^{\text{th}}$. Likewise, to the Gilbert damping there corresponds an effective thermal magnetic field [70] $\mathbf{B}^{\text{th}}$, which modifies the Gilbert torque by

$$\boldsymbol{\tau}_i^\alpha = \boldsymbol{\tau}_i^\alpha\big|_{T=0} + \boldsymbol{\mu}_i \times \mathbf{B}_i^{\text{th}}. \qquad (18)$$

These are stochastic vectors with zero mean, i.e.,

$$\langle \mathbf{B}_i^{\text{th}} \rangle = \langle \mathbf{F}_i^{\text{th}} \rangle = \langle \boldsymbol{\tau}_i^{\text{th}} \rangle = \mathbf{0}, \qquad (19)$$

where $\langle \ldots \rangle$ is an ensemble average in thermal equilibrium. We assume no correlation in the fluctuations of different MNPs, e.g., $\langle B_{i,\alpha}^{\text{th}} B_{j,\beta}^{\text{th}} \rangle \sim \delta_{ij}$ where δ_{ij} is the Kronecker delta, and $\alpha, \beta \in \{x, y, z\}$ denote vector components. We furthermore assume that each vector component is described by a Gaussian distribution with no correlation from one point in time to another (no autocorrelation). This is justified for $\mathbf{B}^{\text{th}}$ in general [70], and for $\mathbf{F}^{\text{th}}$, $\boldsymbol{\tau}^{\text{th}}$ whenever the MNPs are much larger and slower than the fluid particles [55]. That is because on the characteristic timescales of MNP motion, there are enough random collisions with fluid particles that the central limit theorem applies (Gaussian distribution) and the time between consecutive impacts is negligible (again, no autocorrelation). It may then be shown that for a given MNP [70]

$$\langle B_\alpha^{\text{th}}(t) B_\beta^{\text{th}}(t') \rangle = \frac{2k_B T \alpha}{\gamma\mu}\delta_{\alpha\beta}\delta(t-t') \qquad (20)$$

and [71,72]

$$\langle F_\alpha^{\text{th}}(t) F_\beta^{\text{th}}(t') \rangle = 2k_B T \zeta^{\text{t}}\delta_{\alpha\beta}\delta(t-t'), \qquad (21)$$

$$\langle \tau_\alpha^{\text{th}}(t) \tau_\beta^{\text{th}}(t') \rangle = 2k_B T \zeta^{\text{r}}\delta_{\alpha\beta}\delta(t-t'), \qquad (22)$$

where k_B is Boltzmann's constant. $\delta_{\alpha\beta}$ signifies that different vector components are uncorrelated, which is true in Eqs. (21) and (22) only for spherical particles [73–75].

E. Full Langevin dynamics

Here we present the general equations of motion for our Langevin dynamics model of interacting MNPs. Inserting Eqs. (4), (9), (18), and (15) in Eq. (14) yields the LLG equation

$$\dot{\mathbf{m}}_i = -\gamma\mathbf{m}_i \times \mathbf{B}_i^{\text{eff}} + \alpha\mathbf{m}_i \times \dot{\mathbf{m}}_i, \qquad (23)$$

where

$$\mathbf{B}_i^{\text{eff}} = \mathbf{B}_i^{\text{ext}} + \mathbf{B}_i^{\text{dip}} + \mathbf{B}_i^{\text{ani}} + \mathbf{B}_i^{\text{th}} - \alpha\mathbf{m}_i \times \mathbf{B}_i^{\text{Bar}} \qquad (24)$$

is an effective magnetic field. $\mathbf{B}^{\text{ext}}$ is a uniform applied field and the other component fields are given in Eqs. (1), (12), (16), and (20). We emphasize that only $\mathbf{B}^{\text{dip}}$ and $\mathbf{B}^{\text{ext}}$ are actual magnetic fields governed by Maxwells equations. In Appendix A we isolate $\dot{\mathbf{m}}_i$ in Eq. (23), which yields

$$\dot{\mathbf{m}}_i = -\gamma'\mathbf{m}_i \times \mathbf{B}_i^{\text{eff}} - \alpha\gamma'\mathbf{m}_i \times \left[\mathbf{m}_i \times \mathbf{B}_i^{\text{eff}}\right], \qquad (25)$$

where $\gamma' = \gamma/(1+\alpha^2)$.

The mechanical equations of motion are (cf. Appendix B for intermediate steps)

$$I\dot{\boldsymbol{\omega}}_i = \mu\gamma^{-1}\dot{\mathbf{m}}_i + \mu\mathbf{m}_i \times \mathbf{B}_i - \zeta^{\text{r}}\boldsymbol{\omega}_i + \boldsymbol{\tau}_i^{\text{th}}, \qquad (26)$$

$$\mathrm{m}\dot{\mathbf{v}}_i = \mathbf{F}_i^{\text{dip}} - \zeta^{\text{t}}\mathbf{v}_i + \mathbf{F}_i^{\text{th}}, \qquad (27)$$

$$\dot{\mathbf{u}}_i = \boldsymbol{\omega}_i \times \mathbf{u}_i, \quad \dot{\mathbf{r}}_i = \mathbf{v}_i, \qquad (28)$$

where $\mathbf{F}^{\text{dip}}$ is given in Eq. (13) and $\mathbf{B}_i = \mathbf{B}^{\text{ext}} + \mathbf{B}_i^{\text{dip}}$ is the magnetic field from all sources outside MNP i. For a given initial state specified by $\mathbf{m}_i, \mathbf{u}_i, \boldsymbol{\omega}_i, \mathbf{r}_i, \mathbf{v}_i$, the time evolution of the system is fully described by Eqs. (25)–(28).

Equation 25 can alternatively be written

$$\dot{\mathbf{m}}_i = \boldsymbol{\Omega}_i \times \mathbf{m}_i, \quad \boldsymbol{\Omega}_i = \gamma' \mathbf{B}_i^{\text{eff}} + \alpha \gamma' \mathbf{m}_i \times \mathbf{B}_i^{\text{eff}}, \quad (29)$$

where $\boldsymbol{\Omega}$ is the angular velocity of the magnetic moments. This nonstandard form highlights the similarity between the LLG and mechanical rotation, making comparison easier.

III. CONSERVATION LAWS

A. Angular momentum transfer

We consider the change in angular momentum (see Sec. II B 1), given the equations of motion (25)–(28).

For the intrinsic angular momentum of a single MNP, we find

$$\dot{\mathbf{S}}_i = -\gamma^{-1} \dot{\boldsymbol{\mu}}_i, \quad (30)$$

$$\dot{\mathbf{L}}_i = \gamma^{-1} \dot{\boldsymbol{\mu}}_i - \zeta^{\text{r}} \boldsymbol{\omega}_i + \boldsymbol{\mu}_i \times \mathbf{B}_i + \boldsymbol{\tau}_i^{\text{th}}, \quad (31)$$

$$\dot{\mathbf{J}}_i = -\zeta^{\text{r}} \boldsymbol{\omega}_i + \boldsymbol{\mu}_i \times \mathbf{B}_i + \boldsymbol{\tau}_i^{\text{th}}. \quad (32)$$

Note that regardless of the exact dynamics of the magnetic moment, described by $\dot{\boldsymbol{\mu}}_i$, the change in $\mathbf{S}_i$ is compensated by the torque

$$\boldsymbol{\tau}_i^{\text{EdH}} = -\dot{\mathbf{S}}_i = \gamma^{-1} \dot{\boldsymbol{\mu}}_i. \quad (33)$$

Thus, the only ways $\mathbf{J}_i$ can change are by viscous friction or coupling to external fields. The effective fields $\mathbf{B}_i^{\text{ani}}$, $\mathbf{B}_i^{\text{th}}$, and $\mathbf{B}_i^{\text{Bar}}$ can only convert between magnetic and mechanical angular momentum within the ith MNP, so their exact form, and whether they are included in the model, is irrelevant for $\mathbf{J}$ conservation.

We dub $\boldsymbol{\tau}^{\text{EdH}}$ the Einstein–de Haas torque because it produces the Einstein–de Haas effect, i.e., changes in magnetization induce rotation. $\boldsymbol{\tau}^{\text{EdH}}$ bears a striking resemblance to the Barnett field equation (16) because they are two sides of the same phenomenon, namely, that angular momentum conservation necessitates a direct coupling between magnetic and mechanical rotation. We note that if the MNPs are fixed inside a solid, the $\boldsymbol{\tau}^{\text{EdH}}$ and $\boldsymbol{\mu}_i \times \mathbf{B}_i$ torques are transferred to the surrounding material so the whole sample rotates, which leads to the macroscopic Barnett and Einstein–de Haas effects.

The change in total angular momentum is

$$\begin{aligned}
\dot{\mathbf{J}} &= \sum_i (\dot{\mathbf{J}}_i + \mathbf{r}_i \times \dot{\mathbf{p}}_i) \\
&= \sum_i \left(\mathbf{r}_i \times \mathbf{F}_i^{\text{dip}} + \boldsymbol{\mu}_i \times \mathbf{B}_i^{\text{dip}} + \boldsymbol{\mu}_i \times \mathbf{B}_i^{\text{ext}} \right. \\
&\quad \left. - \zeta^{\text{t}} \mathbf{r}_i \times \mathbf{v}_i - \zeta^{\text{r}} \boldsymbol{\omega}_i + \boldsymbol{\tau}_i^{\text{th}} + \mathbf{r}_i \times \mathbf{F}_i^{\text{th}} \right).
\end{aligned}$$

The first two terms are identical to the case of magnetic point dipoles alone in vacuum. This can be verified by repeating the above calculation using Eqs. (9)–(11) at $B^{\text{ext}} = 0$. We prove in Appendix C that this contribution is 0. Thus,

$$\begin{aligned}
\dot{\mathbf{J}} = \sum_i \big(&\boldsymbol{\mu}_i \times \mathbf{B}_i^{\text{ext}} - \zeta^{\text{r}} \boldsymbol{\omega}_i - \zeta^{\text{t}} \mathbf{r}_i \times \mathbf{v}_i \\
&+ \boldsymbol{\tau}_i^{\text{th}} + \mathbf{r}_i \times \mathbf{F}_i^{\text{th}} \big).
\end{aligned} \quad (34)$$

The first term describes coupling to external $\mathbf{B}$ fields, which is in general nonzero. Consider for instance a single dipole in a uniform applied field. The next two describe losses to viscous friction and the last two thermal transfer between MNPs and

fluid particles. In conclusion, the model is indeed angular momentum conserving, except for entirely physical transfer to and from the environment.

We note that the argument relies on the cancellation of $\sum_i \boldsymbol{\mu}_i \times \mathbf{B}_i^{\text{dip}}$ and $\sum_i \mathbf{r}_i \times \mathbf{F}_i^{\text{dip}}$. The former is the change in intrinsic angular momentum of individual MNPs from dipole torques. The latter is the change in extrinsic angular momentum from dipole forces, i.e., the contribution from the MNPs velocity relative to a shared center of mass. Thus, the dynamics of interacting dipoles conserve angular momentum when and only when one considers both rotational and translational degrees of freedom.

B. Absence of field momentum

In Sec. III A, we proved that for MNPs isolated in vacuum, our model conserves the vector $\mathbf{J}$, which is the sum of mechanical and magnetic angular momentum (see Sec. II B 1). However, in the context of electrodynamics, linear and angular momentum are conserved only when also accounting for momentum in the electromagnetic fields and the effect of "hidden momentum" [76–78]. For instance, the net field angular momentum is $\mathbf{J}^{\text{EM}} = \epsilon_0 \int \mathbf{r} \times (\mathbf{E} \times \mathbf{B}) d\mathbf{r}$ where ϵ_0 is vacuum permittivity and $\mathbf{E}$ is electric field [60].

As the MNPs move, their dipole fields change, inducing an $\mathbf{E}$ field; so why did we not need to account for field momentum? The answer is that we calculate all magnetic interactions using magneto*statics*. That is, we both neglect relativistic effects like hidden momentum and induced $\mathbf{E}$ fields. Christiansen *et al.* [79] found that induced $\mathbf{E}$ fields from moment precession in single-domain MNPs are indeed weak compared to other nanoscale induction phenomena. With these approximations, forces, torques, and EM fields are the same as if the instantaneous current distribution was steady.

For a formal proof of angular momentum conservation in electrodynamics, we refer to [[80], problem 6.10]. In Appendix C we modify the argument in [80] to prove that linear and angular momentum are conserved for any steady current distribution when $\mathbf{E} = 0$, without any momenta in the fields. Magnetic dipoles are equivalent to infinitesimal current loops, so the proof applies to MNPs.

This begs a second question: If the external field $\mathbf{B}^{\text{ext}}$ cannot gain or lose momentum, how can it exert forces and torques on the MNPs? The answer is that $\mathbf{B}^{\text{ext}}$ is itself generated by a current distribution, typically in a coil, and the dipole fields from the MNPs exert corresponding forces and torques on this current distribution, ensuring momentum balance.

Finally, we note that if the MNPs have ionizable surface groups or are dispersed in polar solvent, they may carry a surface charge, in which case even the static EM fields carry momentum [81]. Then $\mathbf{L}^{\text{EM}}$ changes as electric charges and magnetic dipoles rearrange, which is exactly balanced by mechanical torques. Whether these torques are significant is beyond the scope of this study.

C. Linear momentum transfer

The change in system linear momentum is

$$\dot{\mathbf{p}} = \sum_i \dot{\mathbf{p}}_i = \sum_i \mathfrak{m}_i \dot{\mathbf{v}}_i$$

which is given in Eq. (27). $\mathbf{F}^{\text{dip}}$ is given by a pairwise, velocity-independent potential, hence it obeys Newtons third law. It follows that

$$\dot{\mathbf{p}} = \sum_i \left(-\zeta^{\text{t}} \mathbf{v}_i + \mathbf{F}_i^{\text{th}} \right). \tag{35}$$

That is, linear momentum is conserved except for viscous friction and Brownian forces, i.e., momentum exchange with the fluid particles.

D. Energy transfer

The equations of motion (9)–(11) and (28) by construction conserve the system energy [Eq. (7)]. For the complete model with damping and fluctuations [Eqs. (25)–(28)], we find after considerable algebra (see Appendix D)

$$\dot{E} = \sum_i \left(P_i^{\text{hyst}} + P_i^{\text{mag}} + P_i^{\text{rot}} + P_i^{\text{trans}} \right), \tag{36}$$

where

$$P_i^{\text{hyst}} = -\mu \mathbf{m}_i \cdot \dot{\mathbf{B}}^{\text{ext}}, \tag{37}$$

$$P_i^{\text{mag}} = -\alpha \mu \gamma^{-1} ([\boldsymbol{\Omega}_i - \boldsymbol{\omega}_i] \times \mathbf{m}_i)^2$$
$$+ \mu[(\boldsymbol{\Omega}_i - \boldsymbol{\omega}_i) \times \mathbf{m}_i] \cdot \mathbf{B}_i^{\text{th}}, \tag{38}$$

$$P_i^{\text{rot}} = -\zeta^{\text{r}} \omega_i^2 + \boldsymbol{\omega}_i \cdot \boldsymbol{\tau}_i^{\text{th}}, \tag{39}$$

$$P_i^{\text{trans}} = -\zeta^{\text{t}} v_i^2 + \mathbf{v}_i \cdot \mathbf{F}_i^{\text{th}}. \tag{40}$$

$\dot{E}$ is the net energy transfer between the MNPs and their environment. By environment we mean both the liquid or solid medium, the external currents generating $\mathbf{B}^{\text{ext}}$, and internal degrees of freedom in the particles, like electronic states and lattice vibrations. $\dot{E} > 0$ means the MNPs are gaining energy while $\dot{E} < 0$ means they are losing energy to the environment.

The hysteresis power P^{hyst} describes the power absorbed by the magnetic moments from $\mathbf{B}^{\text{ext}}$. As shown in Eq. (42), the area of a hysteresis curve measures the time- and system-averaged value of P^{hyst}, hence the name. P^{hyst} is the main source of energy into the MNP system, while the other terms generally dissipate this energy into the environment.

P^{rot}, P^{trans} describe exchange of kinetic energy with the fluid medium, so the resulting viscous losses go to heating the surrounding fluid. P^{mag} describes Gilbert damping, i.e., energy transfer from the single-domain moments to internal degrees of freedom like phonon modes [82], spin waves [82], and electronic transitions [83]. We observe that P^{mag} depends on the difference in angular velocity between mechanical and moment rotation, so Gilbert damping is given by changes in moment orientation *relative* to the particles' atomic lattice. Gilbert damping heats the MNPs themselves.

While there is thermal conduction between MNPs and fluid, a nonuniform temperature profile is possible in driven systems even in equilibrium. The magnitude of both viscous and magnetic losses combined with heat transfer mechanisms will determine the shape of this profile.

When setting $\omega_i = 0$, Eq. (38) is in complete agreement with Ref. [[49], Eq. (6)], which included the thermal power, but did not consider mechanical motion. To show the equivalence, one may use the identity $|\boldsymbol{\Omega} \times \mathbf{m}|^2 = \gamma \gamma' |\mathbf{B}^{\text{eff}} \times \mathbf{m}|^2$.

Equations (39) and (40) are consistent with known expressions for rigid-body particles in fluid [84,85].

For P^{mag}, P^{rot}, and P^{trans}, the first term is pure damping, while the second describes a two-way transfer from thermal fluctuations. Over time, thermal fluctuations will typically average to 0, but at a given instant, there may be a net energy transfer from environment to system. The two terms are related by the fluctuation-dissipation theorem [55], so if α, ζ^{r} or ζ^{t} is zero, the corresponding fluctuations are absent, in which case P^{mag}, P^{rot}, or P^{trans}, respectively, is 0.

Each damping mechanism is local, so P_i^{mag} changes the internal temperature of the ith MNP and P_i^{rot}, P_i^{trans} heat the fluid in the vicinity of the ith MNP. That said, the distribution of power dissipation in the fluid would require further analysis. Also, some of the viscous dissipation may heat the MNP surface directly, as the surface inelastically collides with fluid particles. Likewise, by tracking the dissipation of momenta, one can infer how much the MNP motion stirs the fluid, but not the exact form of waves and vortices formed.

1. Hysteresis curve comparison

Consider if $\mathbf{B}^{\text{ext}}$ is periodic with frequency f_{ext}. Then the time-averaged power absorption is

$$\overline{P^{\text{hyst}}} = -f_{\text{ext}} \int_{\text{cycle}} \mathbf{m}_{\text{total}} \cdot \dot{\mathbf{B}}^{\text{ext}} dt \tag{41}$$

$$= -f_{\text{ext}} \oint_{\text{cycle}} \mathbf{m}_{\text{total}} \cdot d\mathbf{B}^{\text{ext}}. \tag{42}$$

In other words, the average energy gained by the MNPs per field cycle is given by the area of the hysteresis curve, at least when $\mathbf{m}_{\text{total}}(\mathbf{B}^{\text{ext}})$ forms a closed curve. All of this energy is eventually dissipated as heat, so the hysteresis area is a standard way to estimate heating power [10,11,43]. For an isolated MNP one can even distinguish magnetic losses by computing the hysteresis curve in a local, coordinate system that follows the mechanical rotation, as done in Ref. [45].

The hysteresis area approach has several limitations. The $\mathbf{m}_{\text{total}}(\mathbf{B}^{\text{ext}})$ curve must be closed and cyclic, which requires periodic driving and that the system is in steady state, or at least changes slowly relative to f_{ext}. It gives a time-averaged power, so f_{ext} limits time resolution. Also, it only gives the absorbed power averaged over all particles so there is no information on where and how the energy is dissipated. In simulations, one can compute the hysteresis curve of each MNP, but this does not account for the dipolar fields and other interactions. Because interactions transfer energy between MNPs, the work done by $\mathbf{B}^{\text{ext}}$ on MNP i may be dissipated elsewhere. Therefore, as discussed in Refs. [14,15,49], hysteresis curves cannot determine local heating in interacting systems.

Using Eqs. (37)–(40) directly gives a local perspective on the instantaneous power, both input and loss channels, which also works for transient and nonequilibrium dynamics of interacting MNP systems. If coupled to a model of heat transfer, one can in principle simulate the entire temperature distribution. Also plotting Eqs. (37)–(40) vs time gives an alternative way to visualize and interpret various MNP dynamics, as we demonstrate in Sec. V.

TABLE I. Typical parameter ranges for modeling single-domain MNPs made from Fe, Co, Ni, and their oxides.

Symbol	Description	Unit	Values
γ	Gyromagnetic ratio	$s^{-1} T^{-1}$	1.76×10^{11}
R	Radius	nm	1..50
T	Temperature	K	$0 \dots 1400$
η	Dynamic viscosity	kg/(m s)	$\geqslant 10^{-3}$
ρ	Mass density	g/cm^3	$1 \dots 10$
M	Magnetization	A/m	$10^5 \dots 10^6$
B_{ext}	Applied field magnitude	T	0...1
f_{ext}	Applied field frequency	Hz	$0 \dots 10^7$
K	Anisotropy energy density	J/m^3	$10^3 \dots 10^6$
α	Gilbert damping	1	$10^{-3} \dots 0.5$

IV. MODEL APPROXIMATIONS

Equations (25) to (28) constitute a highly general, numerically solvable model for the dynamics of an MNP collection. It can be used to study aggregation, hysteresis, magnetic susceptibility, Brownian diffusion, moment-dynamics in clusters, etc. The price is heavy computations, with little hope for analytical solutions, therefore it is common to consider approximate models. Here we discuss several useful approximations in the context of conservation laws.

A. Parameter ranges

In Table I we list the model parameters, including typical ranges in MNP studies for ferromagnetic and ferrimagnetic nanoparticles.

Spherical MNPs typically cease to be single domain at [86] $R = 50$ nm or less, with some notable exceptions for rare-earth compounds [87]. Studies are typically conducted at room or body temperature for biomedical applications, but $T = 950\,°\text{C}$ has been tested for catalysis [2] and the Curie temperature of Co is 1400 K. Water, as one of the least viscous liquids, has $\eta = 1.0$ mPa s at $T = 300$ K. Typical MNP materials are iron oxides for biomedicine, e.g., maghemite ($\gamma-\text{Fe}_2\text{O}_3$), and metals like Fe and Co for catalysis. The bulk, saturation magnetizations are $M_s^{\text{Fe}_2\text{O}_3} = 412$ kA/m, $M_s^{\text{Co}} = 1.4$ MA/m, and $M_s^{\text{Fe}} = 1.7$ MA/m, however, the magnetization of nanomagnets is typically smaller than bulk due to disordered surface spins [88]. The same surface effects increase the effective anisotropy constant for very small particles [89]; for example [90], $K = 20$ kJ/m^3 has been estimated for bulk maghemite but for $R = 2$ nm particles experimental results are around $K = 90$ kJ/m^3.

Using ferromagnetic resonance Bhagat and Lubitz [91] measured the Gilbert damping in monocrystalline, bulk Fe, Co, and Ni as a function of temperature. Reading off their relaxation parameter at $T = 300$ K and multiplying by [92] $4\pi/(\mu_0\gamma M_s)$ to convert to α, the results are $\alpha_{\text{Fe}} = 2.2 \times 10^{-3}$, $\alpha_{\text{Co}} = 3.5 \times 10^{-3}$, and $\alpha_{\text{Ni}} = 2.5 \times 10^{-2}$. By doping NiFe thin films $\alpha_{\text{NiFe}} = 0.1$ has been measured at 300 K [93]. At the other end of the scale is yttrium-iron-garnet (YIG), which for a monocrystalline, $R = 300$ μm sphere was found to have [94] $\alpha_{\text{YIG}} = 2.7 \times 10^{-5}$. In summary, α is generally $\ll 1$ with typical values around 10^{-3} to 10^{-2} and outliers down to

less than 10^{-4}. However when simulating phenomena with a weak α dependence, one can speed up magnetic relaxation by using α near unity, thus potentially reducing computation time.

When two MNPs are in surface contact, the field from one at the center of the other is

$$B_{\text{contact}}^{\text{dip}} = \frac{\mu_0 \mu}{16\pi R^3} = \frac{1}{12}\mu_0 M$$

which ranges from 1 to 100 mT for the considered magnetizations. Thus, it is case specific whether the external field exceeds the dipole field.

For reference, the mass, moment of inertia, and magnetic moment of a spherical, single-domain magnet are $\mathfrak{m} = \frac{4\pi}{3}\rho R^3$, $I = \frac{8\pi}{15}\rho R^5$, and $\mu = \frac{4\pi}{3}MR^3$, respectively. Friction coefficients are given in Eq. (17).

B. Overdamped limit

For micron scale and smaller objects moving in liquid, inertia tends to be negligible [56]. The argument is that viscous drag dampens away transient responses so quickly that objects are essentially always moving at terminal velocity. Therefore, in Langevin dynamics studies of microswimmers, the inertia term is traditionally neglected [95]. For MNPs, torques and forces can change on ns timescales or faster due to moment precession [39], so it is not immediately clear if inertia can always be neglected, and it has been shown to greatly affect the rotation of macroscopic coupled dipoles [96]. That said, some studies [43], including our own in Sec. V, have found no apparent difference between the MNP trajectories for simulations with or without inertia.

In the overdamped limit ($\mathfrak{m}, I \to 0$) Eqs. (26) and (27) reduce to

$$\zeta^{\text{r}}\boldsymbol{\omega}_i = \mu\gamma^{-1}\dot{\mathbf{m}}_i + \mu\mathbf{m}_i \times \mathbf{B}_i + \boldsymbol{\tau}_i^{\text{th}}, \qquad (43)$$

$$\zeta^{\text{t}}\mathbf{v}_i = \mathbf{F}_i^{\text{dip}} + \mathbf{F}_i^{\text{th}}, \qquad (44)$$

while Eqs. (25), (28), and (29) remain unchanged. Then linear and angular velocities ($\mathbf{v}, \boldsymbol{\omega}$) are given by the *immediate* forces and torques, so the system state is specified just by $\mathbf{m}_i, \mathbf{u}_i, \mathbf{r}_i$.

The power expressions (37)–(40) are formally unchanged, while $\dot{\mathbf{p}} = \dot{\mathbf{L}} = 0$. The reason is that the transient, inertial dynamics are approximated as decaying infinitely quickly, so the system is always in force and torque balance. In this case one can still calculate momenta directly from $\mathbf{v}(t)$ and $\boldsymbol{\omega}(t)$, but Eqs. (31), (32), and (34) are pointless.

1. Characteristic frequencies

In the overdamped limit we can easily determine characteristic frequency scales. For numerical estimates, we consider the parameter ranges in Table I. Using that $\alpha \ll 1$ we have $\gamma' \approx \gamma$, so $\Omega \sim \gamma B^{\text{eff}}$ which is the well-known Larmor frequency for moment precession. For mechanical rotation, inserting Eq. (25) in (43) yields $\zeta^{\text{r}}\omega \sim \mu B^{\text{ani}} + \alpha\mu B^{\text{eff}}$. If $\alpha B^{\text{eff}} \lesssim B^{\text{ani}}$ then $\omega \sim \mu B^{\text{ani}}/\zeta^{\text{r}} \sim K/(3\eta)$, which ranges from 300 kHz to 300 MHz in water. In general, $\omega \lesssim \mu B^{\text{eff}}/\zeta^{\text{r}}$, so whenever the overdamped limit is applicable

$$\frac{\omega}{\Omega} \lesssim \frac{\mu}{\gamma \zeta^{\text{r}}} = \frac{M}{6\gamma\eta} \leqslant 0.001.$$
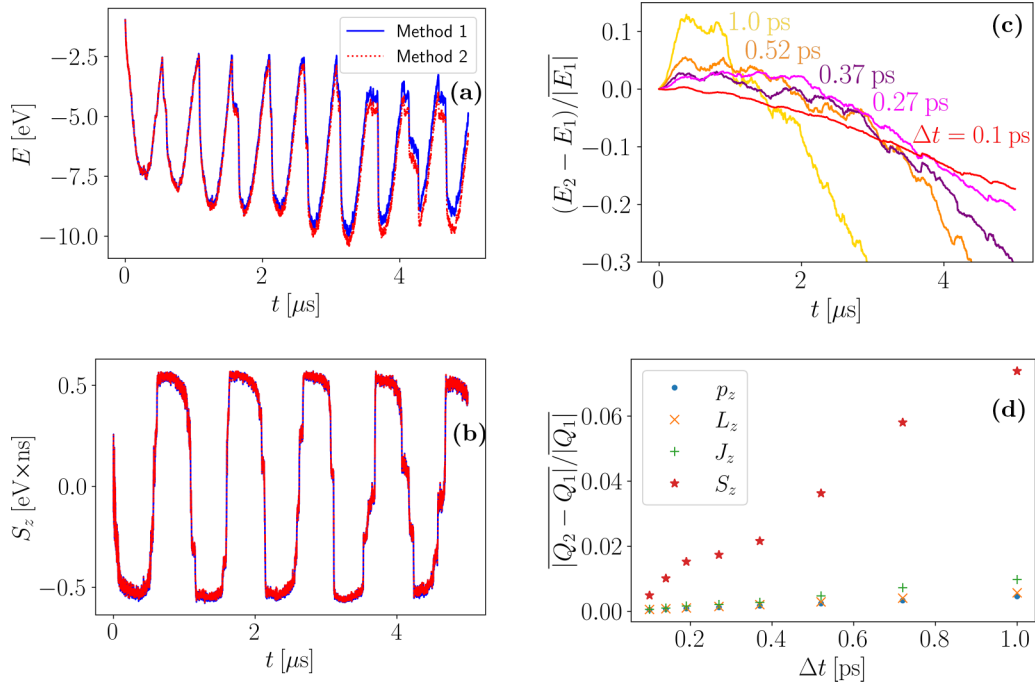
FIG. 2. Conservation law tests. The test system is 10 MNPs with $R = 10$ nm, $M = 400$ kA/m, $K = 10$ kJ/m^3, $\rho = 4.9$ g/cm^3, and $\alpha = 0.01$ dispersed in liquid with $\eta = 1$ mPa s and $T = 300$ K. There is an external field of the form $\mathbf{B}^{\text{ext}} = B^{\text{ext}} \sin(2\pi f^{\text{ext}} t)\mathbf{e}_z$ where $B^{\text{ext}} = 50$ mT and $f^{\text{ext}} = 1$ MHz. The maximal anisotropy field strength is then $B^{\text{ani}}_{\max} = 2K/M = 50$ mT. Initial conditions are random with a volume fraction of 0.1, but the same across all simulations. An equivalent initial state is seen in Fig. 4(c). (a), (b) System energy and z component of magnetic angular momentum in $\Delta t = 0.1$ ps simulations, evaluated with both method 1 (direct evaluation) and method 2 (integration of time derivative). (c) Relative difference between E_2 and E_1 vs time at different time steps. (d) Average error in z components of system momenta vs time step for method 2 relative to method 1. $\overline{Q}$ refers to a time average over the whole 5-μs simulation, where Q is a placeholder for p_z, L_z, J_z, and S_z. (b), (d) Include inertia for tracking momentum but in (a) and (c) the overdamped limit is used and kinetic energy is excluded. For each data point, the method 1 and 2 estimates are from the same simulation, so the thermal noise is identical. The simulation in a) is animated in the Supplemental Material [57].

We conclude that for any overdamped MNP system in the parameter space of Table I, mechanical rotation is at least three orders of magnitude slower than moment precession.

The characteristic rate of magnetic relaxation is [39] $\alpha\Omega$ which also exceeds ω for all parameter combinations in Table I. Both magnetic frequency scales are apparent in Fig. 3.

2. Neglecting the Barnett field

For the Barnett field (16), we have

$$\frac{B^{\text{Bar}}}{B^{\text{eff}}} \sim \frac{\omega}{\Omega} \leqslant 0.001.$$

Thus, for typical MNP simulations in liquid, the Barnett field is a tiny correction to $\mathbf{B}^{\text{eff}}$ and, as pointed out in Sec. III A, it does not change whether angular momentum is conserved. Similarly, one can to a good approximation set $\omega = 0$ in Eq. (38), i.e., calculate P^{mag} in laboratory coordinates rather than local coordinates. While this vindicates previous numerical studies, e.g. [39,42,45,47,97], we find that using the exact expressions does not significantly increase computational complexity.

For MNPs suspended in vacuum or low-density gas, the mechanical rotation can be much greater, so the above argument breaks down. Indeed, in low friction conditions the Barnett field has been theorized to produce additional lines

in a ferromagnetic resonance spectrum [25], and to enable stable levitation of a nanomagnet even in a static applied field [51,54]. Also, by rapidly rotating dried and frozen samples of Fe$_3$O$_4$ nanoparticles the Barnett field has been measured with enough accuracy to infer orbital corrections to the gyromagnetic ratio [53]. To simulate near-vacuum conditions, one may use the full inertial model with a low value of the friction coefficient η.

C. Rigid dipole approximation

The popular rigid dipole approximation (RDA) [32,44,98] says that the moment is locked to the mechanical rotation of the particle, i.e., $\mathbf{m} = \mathbf{u}$. Then Eq. (25) drops out, α is no longer a model parameter, and Eq. (26) reduces to

$$I\dot{\boldsymbol{\omega}}_i + \zeta^{\text{r}}\boldsymbol{\omega}_i = \mu\gamma^{-1}\dot{\mathbf{u}}_i + \mu\mathbf{u}_i \times \mathbf{B}_i + \boldsymbol{\tau}^{\text{th}}_i \quad \text{(RDA)}.$$

Using that $\dot{\mathbf{u}} = \boldsymbol{\omega} \times \mathbf{u}$ this can be rewritten

$$I\dot{\boldsymbol{\omega}}_i + \zeta^{\text{r}}\boldsymbol{\omega}_i = +\mu\mathbf{u}_i \times (\mathbf{B}_i + \mathbf{B}^{\text{Bar}}_i) + \boldsymbol{\tau}^{\text{th}}_i \quad \text{(RDA)}.$$

Typically, the $\dot{\mathbf{u}}_i$ term is also neglected, which evidently is equivalent to neglecting the Barnett field, hence justified in liquid suspension.

Because you avoid the high-frequency moment dynamics, the RDA enables a major increase in simulation speed, and facilitates analytical solutions [44]. The power expressions
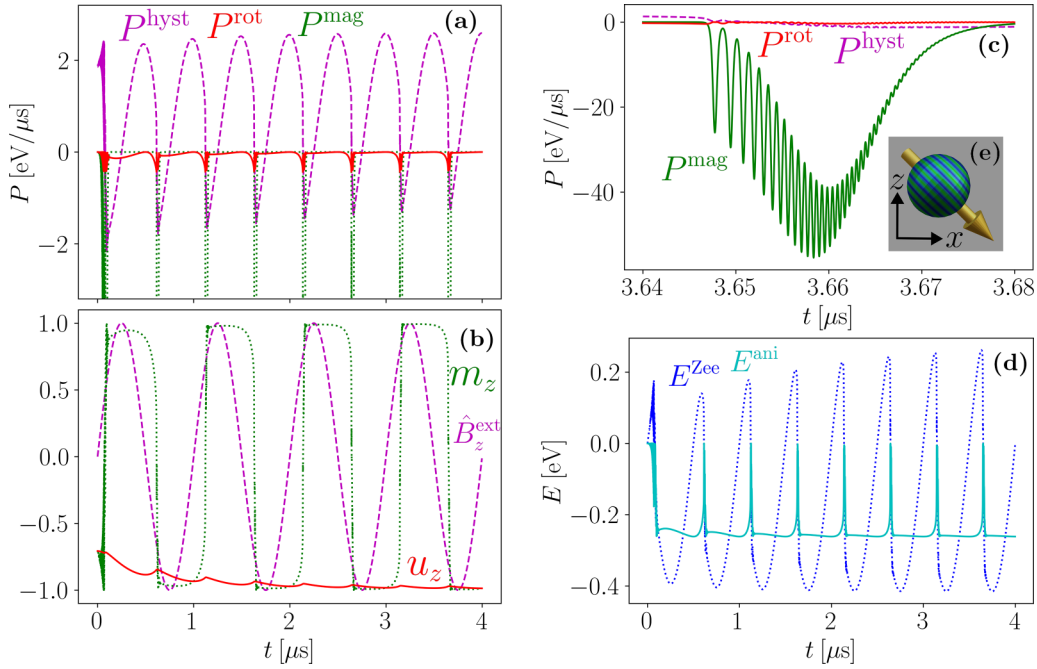
FIG. 3. Single MNP in liquid. Same parameters as in Fig. 2 except $T = 0$ and $B^{\text{ext}} = 40$ mT. The initial state is shown in (e) and given by $\mathbf{m} = \frac{1}{\sqrt{2}}(1, 0, -1)$, $\mathbf{u} = \frac{1}{\sqrt{2}}(-1, 0, -1)$. The plots are identical for inertial and overdamped simulations. (a), (c) Energy transfer vs time, decomposed into Gilbert damping, rotational viscous damping, and power absorbed from the driving field. (a) Shows the full 4 μs but a subset of the power axis for clarity, while (c) shows a 40-ns zoom onto the last moment reversal. (b) Same simulation in terms of the z components of the normalized moment $\mathbf{m}$, orientation vector $\mathbf{u}$, and driving field $\hat{\mathbf{B}}^{\text{ext}}$. (d) Energy decomposed into Zeeman and anisotropy energies. Both the full simulation and the zoom in c) are animated in the Supplemental Material [57].

Eqs. (36), (37), (39), and (40) are unchanged but $P^{\text{mag}} = 0$, i.e., Gilbert damping is excluded from the model.

The RDA relies on two assumptions: (1) that transient, moment dynamics are irrelevant for the phenomenon of interest and (2) that $\mathbf{B}^{\text{eff}}$ is dominated by $\mathbf{B}^{\text{ani}}$ so that $\mathbf{m} \| \mathbf{u}$ in steady state. We refer to Ref. [44] for further analysis of when and why the RDA is applicable.

In some regimes, even though $\mathbf{m} \| \mathbf{u}$ is nearly true most of the time, Gilbert damping is the primary loss channel [42,45], so the RDA should be applied with great care when studying energy transfer. An example is seen in Fig. 3. Conversely, we also present a simulation of zero-field aggregation in Fig. 4 where the RDA would have been reasonable.

D. Immobilized particles

Consider a collection of MNPs immobilized in a solid substrate, i.e., no mechanical rotation or translation possible. Then $\mathbf{B}^{\text{Bar}}$, P^{rot}, $P^{\text{trans}} = 0$ and Eqs. (26)–(28) drop out of the model, leaving just the LLG part [Eq. (25)]. $\mathbf{r}_i$, $\mathbf{u}_i$ are constants which still enter through $\mathbf{B}_i^{\text{dip}}$ and $\mathbf{B}_i^{\text{ani}}$ respectively, but $\mathbf{m}_i$ are the only dynamical variables. Then the model is essentially an example of micromagnetics.

V. SIMULATIONS

A. Method

1. Time-step integration

To simulate the derived model, our method of choice is time-step integration. The core idea is to discretize time into

steps of Δt which are short compared to all characteristic timescales in the system. This justifies a number of numerical schemes for updating the configuration from t to $t + \Delta t$. By iteratively updating the system, its entire time evolution is evaluated.

In addition to the model in Sec. II E we include the Weeks-Chandler-Andersen (WCA) force:

$$\mathbf{F}_i^{\text{WCA}} = \sum_{j \neq i} \begin{cases} 12\epsilon_{\text{WCA}}\left[\frac{(2R)^{12}}{r_{ji}^{13}} - \frac{(2R)^6}{r_{ji}^7}\right], & r_{ji} \leqslant 2R \\ 0, & r_{ji} > 2R \end{cases} \tag{45}$$

and associated potential, as in [32]. This purely repulsive force only takes effect when two particles are in contact, hence, its sole impact on the dynamics is to prevent particle overlap so the code can handle collisions. We use $\epsilon_{\text{WCA}} = 10^{-19}$ J throughout, which produces a relatively tiny contribution to the system energy [see Fig. 4(b)].

We present our algorithms in Appendix E. The mechanical equations [(26) and (27)] are second order with inertia but first order in the overdamped limit, so two different algorithms are needed. We use the simple Euler method for updating position, velocity, etc., and the Euler-Rodriguez formula for rotations [99] because it is exceedingly good at conserving vector magnitudes. For moment rotations, we also tested a combination of Heuns method and the Euler-Rodriguez formula, but for ease of reproducibility all presented data use the simple scheme.

One can improve performance by various higher-order integrators and adaptive time stepping [29] or symplectic algorithms for the second-order equations [100]. However, there
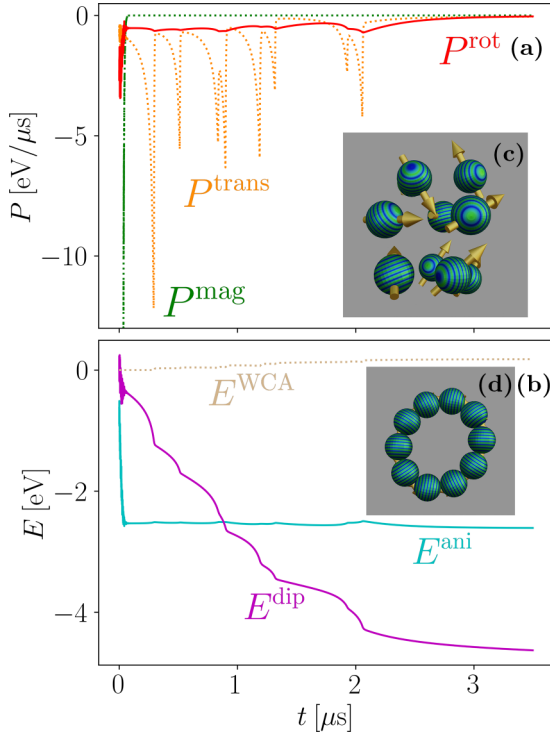
FIG. 4. 10 MNP collision. Same parameters as in Fig. 2, except $T, B^{\text{ext}} = 0$. (a) Dissipated power decomposed into Gilbert damping, rotational, and translational viscous losses. (b) System energy decomposed into anisotropy, WCA, and dipole interaction energy. (c) Initial state. Randomly generated at a volume fraction of 0.1. (d) Final configuration after 15 μs. Only the first 3.5 μs are shown in (a) and (b), because aside from a collision around $t = 10$ μs all the curves are nearly flat after $t = 3.0$ μs. The plots are identical for inertial and overdamped simulations. The simulation is animated in the Supplemental Material [57].

are already a number of technical subtleties when integrating stochastic equations [101], so we prioritized clarity over efficiency.

2. Stochastic integration

Our model is a set of coupled stochastic differential equations (SDEs) because it contains the stochastic vectors $\mathbf{B}^{\text{th}}, \mathbf{F}^{\text{th}}, \boldsymbol{\tau}^{\text{th}}$. Since these have zero autocorrelation [see Eqs. (20)–(22)], they change significantly on an infinitesimal timescale. Therefore, they obey different rules of calculus than the deterministic vectors. See, e.g., [101–103] for an introduction to SDEs and stochastic calculus.

When discretizing time, the closest we can get to zero autocorrelation is to randomize the stochastic vectors every time step. Formally this amounts to the substitution $\delta(t - t') \rightarrow \frac{1}{\Delta t} \delta_{nn'}$ in Eqs. (20)–(22) where n is time-step index. Between updates, the thermal vectors are constant so the time evolution is deterministic. When integrating an SDE like Eq. (34) or (36), it matters at what point in the deterministic intervals the integrand is evaluated because $\dot{\mathbf{S}}$, P^{mag}, P^{rot}, and P^{trans} all contain *multiplicative noise* terms: products of deterministic and stochastic variables like $\mathbf{v} \cdot \mathbf{F}^{\text{th}}$ or $\boldsymbol{\mu} \times \mathbf{B}^{\text{th}}$. If integrated incorrectly, multiplicative noise terms may produce artificial

thermal drift, which is an error proportional to integration time t. Unlike numerical errors from time discretization, thermal noise results from a formal error in the interpretation of an SDE, hence, it remains even as the time step approaches zero.

For continuous processes, as are common in physical systems, the correct choice is often midpoint integration, also known as a Stratonovich integral. However, there are counterexamples. For example, Ref. [104] experimentally studies an electric circuit that can be tuned continuously from Stratonovich calculus to Itô (initial point integration) depending on input parameters. We note that the regular rules of differentiation apply only in Stratonovich calculus, so this is a prerequisite for the derivation of $\dot{E}$ in Appendix D.

Here it should be mentioned that the LLG itself contains multiplicative noise terms. However, it has been shown that the drift is only in the magnitude of magnetic moments [105], so as long as m_i are held constant, one can use all the tools and algorithms for time stepping regular ODEs [29]. For the energy transfer we are not so lucky.

3. Evaluating conserved quantities

For the instantaneous values of energy and momenta at a given time, we simply insert the simulated system configuration in Eqs. (5)–(7). Similarly, the transfer rates are given by Eqs. (34)–(36). This directly gives a way to visualize and interpret MNP dynamics in terms of energy, as we demonstrate in Sec. V C. One caveat is that at finite temperature, the P^{mag}, P^{rot}, and P^{trans} curves tend to be dominated by noise, so we set $T = 0$ in Sec. V C. Also, because MNP mass is neglected in the overdamped limit, we set kinetic energy to 0 for self-consistency.

For practical applications, it is often more informative to consider time averages. For example, for magnetic hyperthermia, the figure of merit is the average power absorption. This can be estimated from the area of the hysteresis curve, but can equivalently be calculated by the time average $\overline{P^{\text{hyst}}} = \frac{1}{t} \int_0^t P^{\text{hyst}}(t') \mathrm{d}t'$. With the present formalism we can likewise average magnetic and viscous loss power, as well as forces and torques.

To model a macroscopic sample, it is more appropriate to consider ensemble averages, say $\langle P \rangle$. By the ergodic hypothesis, $\overline{P}$ is equivalent to $\langle P \rangle$, assuming the system has time to fully explore configuration space. Often MNP systems get stuck in energy minima though, e.g., when aggregating into stable clusters or when the anisotropy barrier KV is large compared to $k_B T$, in which case $\langle P \rangle$ is more efficiently computed by averaging $\overline{P}$ over multiple simulations with different initial conditions.

To test the self-consistency of our analytical results, we consider two different methods for evaluating the total energy and momenta numerically. Method 1 is to take the system configuration directly. For example, in the overdamped case $E_1(t) = E[\mathbf{m}(t), \mathbf{u}(t), \mathbf{r}(t)]$. Method 2 is to integrate the transfer rates, e.g.. $E_2(t) = E(t = 0) + \int_0^t \dot{E}(t') \mathrm{d}t'$ where $\dot{E}$ is given in Eq. (36). The numerical results are presented in Sec. V B and Fig. 2. Method 2 involves the same integral as the time-averaged transfer rates, so the consistency of the two methods at vanishing time step demonstrates the elimination

TABLE II. The conditions where we can integrate power and net linear and angular momentum transfer for the MNP system (method 2). Comparing to direct energy and momenta computations (method 1) is useful for validation of models and benchmarking of numerical implementations.

		Energy	Momenta
Overdamped	$T = 0$	✓	✗
Overdamped	$T > 0$	✓	✗
Inertial	$T = 0$	✓	✓
Inertial	$T > 0$	✗	✓

of thermal drift, and that we can numerically integrate the transfer rates in practice. The comparison can also be used to benchmark a given numerical implementation.

We find that in the overdamped limit, using midpoint integration eliminates thermal drift, so the Stratonovich interpretation is correct and we can integrate all power contributions at finite temperature. This also justifies using the regular rules of differentiation in deriving Eq. (36). As discussed in Sec. IV B, $\dot{\mathbf{p}} = \dot{\mathbf{J}} = 0$ in the overdamped limit, so we cannot compute changes in the MNP momenta. One can still integrate the individual forces and torques, but running our self-consistency test on momenta requires inertia.

$\dot{\mathbf{S}}$ is prone to thermal noise because unlike the single-particle moments the magnitude of $\mathbf{S}$ fluctuates, but midpoint integration works. Thus, with inertia and midpoint integration specifically for $\dot{\mathbf{S}}$ we can integrate all momentum components at finite temperature. However, when integrating the total power with inertia, significant thermal drift is present for both Itô and Stratonovich integration regardless of time step, and we have not found a suitable alternative. It is possible the correct SDE interpretation depends on the magnitude of the inertia, analogously to [104]. See Table II for a summary of when we can integrate the transfer rates.

We note that for all simulations presented in Secs. V B and V C we simulated both the overdamped limit and full, inertial model, and also compared methods 1 and 2 for energy and momenta to the extent it was possible without thermal drift. There was no apparent difference between inertial and overdamped curves, so MNP mass is negligible for all presented simulations.

B. Conservation law tests

In Fig. 2 we compare the two presented methods for computing conserved quantities at different time steps. Note that the test simulations include moment relaxation, an alternating external field, dipole interactions, MNP collisions, and thermal fluctuations in all degrees of freedom, all with experimentally relevant parameter values.

In Fig. 2(a) we see excellent agreement in the energy integration for short times. At longer times, variations in the red and blue curves are still nearly identical over short intervals, but the red is shifted down. This indicates a persistent, erroneous drift in method 2. In Fig. 2(c) we see that regardless of time step, the error increases linearly in time at long time, like thermal drift. But unlike thermal drift the error decreases with decreasing time step, so as $\Delta t \to 0$ the methods con-

verge. Furthermore, using our modified Heuns' method for the moment rotations, the drift is reduced by several orders of magnitude. We conclude that the two integration methods are formally identical and the drift is a purely numerical error. This self-consistency check in turn validates our analytical energy transfer analysis [cf. Eq. (36)].

In Fig. 2(b) we see the time variation in S_z which is proportional to the z component of the systems net moment. Interestingly, while the external driving field is sinusoidal, the moment switches in a steplike manner. In some cases the switching happens in several smaller steps, as thermal fluctuations and dipole- nteractions make some of the 10 MNPs flip before others.

We see excellent agreement between methods 1 and 2 throughout, i.e., midpoint integrating $\dot{\mathbf{S}}$ has eliminated thermal drift and there is no discernible drift from numerical error. Thus, we can meaningfully consider the time-averaged deviation of the two methods for momenta. In Fig. 2(d) it is seen that the methods converge with decreasing time step as expected and at $\Delta t = 0.1$ ps the relative deviation is less than 1%. The same qualitative behavior is found for the x and y components. This validates the analysis in Sec. III, so we conclude that all momenta and momentum transfer in the model is accounted for.

1. The computational bottleneck

With our homemade Python implementation, a 50-particle simulation on a single cpu core runs roughly 10^3 iterations per second. At $\Delta t = 0.1$ ps, as in Fig. 2, this amounts to almost 3 h of cpu time per μs simulated, which limits the timescale and MNP number that can be studied.

The fastest intrinsic timescale is moment precession (cf. Sec. IV B 1), and from Fig. 2(d) we see that the moment dynamics are far more time step sensitive than the mechanical motion. But at say $B_{\mathrm{eff}} = 100$ mT, the precession period is 0.4 ns, which suggests a much longer time step should be possible, e.g., 10 ps.

The limiting factor is the magnetic loss power P^{mag}, which varies at the precession frequency [see Fig. 3(c)] and, unlike P^{hyst}, P^{mag} contains multiplicative noise terms, hence is prone to numerical drift. The issue is exacerbated when the magnetic field $\mathbf{B}$ and anisotropy axis are noncollinear, as both the anisotropy field magnitude $B^{\mathrm{ani}} \sim \mathbf{m} \cdot \mathbf{u}$ and the moment direction then oscillate at the precession frequency, but not in a self-consistent manner. The evaluation of $\mathbf{S}$ in Fig. 2(d) by method 2 is similarly demanding, but one can always compute $\mathbf{S}$ from the individual moments $\boldsymbol{\mu}_i$ (method 1), so integrating $\dot{\mathbf{S}}$ is never required in practice. We only do it for model validation.

For P^{mag} one option is to compute the total energy change directly from Eq. (7), integrate P^{hyst}, P^{rot}, P^{trans}, then use energy conservation to estimate $\int P^{\mathrm{mag}} \mathrm{d}t$. This only works at the system level though, not for the magnetic losses locally at a given particle. To integrate P^{mag} directly at finite temperature and reasonable computational expense, an advanced time-step method is necessary for the moment rotation. For example, with our modified Heuns' method just on moment dynamics, the drift remains, but is reduced by approximately a factor of 100. We recommend comparing energy estimates

from methods 1 and 2 like in Figs. 2(a) and 2(c) for method validation.

C. Example simulations at zero temperature

1. Single-particle hysteresis

Figure 3 shows a single MNP under a sinusoidal driving field. In the first 100 ns we have the transient dynamics of the moment relaxing towards the anisotropy axis, as **m**, **u** start with a 90° relative angle. This results in major magnetic losses (green curve) rapid variation in the energy transfer from the external field (purple curve) and a smaller quantity of viscous losses. In general, magnetic losses are dominant in this parameter regime. Rapid variation is also seen in Zeeman and anisotropy energies (blue and light blue curves, respectively).

The green spikes in Fig. 3 signify moment reversals. Before each reversal, viscous losses increase as the MNP mechanically rotates towards B^{ext} (tails in red curve), but as the field reaches some critical value, the moment flips to the other anisotropy minimum instead. This flip is followed by about 5 ns of precessional motion and associated Gilbert damping, as seen in Fig. 3(b). The reversal events are also marked by spikes in E^{ani}, sudden drops in E^{Zee}, and seen directly on the m_z curve.

We note that P^{mag} oscillates at the precession frequency [green curve in Fig. 3(c)]. The reason is that B^{ani} oscillates when **u** and B^{ext} are noncollinear. Indeed, when the mechanical orientation is fixed with $\mathbf{u} \parallel B^{\text{ext}}$ the oscillations are absent, and their amplitude increases with the angle between **u** and B^{ext}. Interestingly, the precession frequency increases over time as B^{eff} changes. The maximal frequency is about 1.3 GHz which is consistent with the Larmor frequency $\gamma B^{\text{ext}}/(2\pi) = 1.4$ GHz.

The integrated area of $P^{\text{hyst}} = -\mu m_z \dot{B}_z^{\text{ext}}$ is positive in every half-cycle, so there is a net transfer of energy from driving field to MNP. This asymmetry is only possible because the MNP moves in response to the field. In particular, when m_z is positive, B^{ext} is mostly decreasing and for m_z negative, B^{ext} is mostly increasing. Without changes in **u** or **m**, the P^{hyst} and E^{Zee} curves would both follow the B^{ext} curve and average to 0. Indeed, P^{hyst}, E^{Zee} vary sinusoidally between reversal events like B^{ext}.

Over time, the purple curve is shifted upwards, which means the net energy transfer increases both absorption and subsequent dissipation. This is accompanied by an increase in the scale of E^{Zee}. The reason is the gradual relaxation of the anisotropy axis towards vertical ($u_z \to -1$). The corresponding mechanical rotation also explains the viscous losses and E^{ani} changes between reversal events, which are visible in the first 1.5 µs. Finally, we note that reversal events happen twice every field cycle, so all the power and energy contributions have double the frequency of the driving field.

To conclude, while the system energy builds gradually over each half-cycle of the driving field, it is dissipated in the span of a few ns by Gilbert damping. This means the internal temperature of the MNP will increase in sudden jumps, after which the energy is gradually conducted to the surrounding fluid.

This analysis is specific to the chosen parameters, in fact it has been shown in previous numerical studies that viscous, rotational losses dominate in some regimes [42,45]. Also, the number of moment oscillations during magnetic relaxation, and hence the timescale of a reversal event, is proportional to α, which varies greatly between materials.

2. Zero-field aggregation

In Fig. 4 we consider 10 randomly initiated MNPs at zero temperature and no external field. Consequently, no energy is added to the system, so this is a pure relaxation. The particles are initiated randomly as seen in Fig. 4(c), form into a single chain within the first 3 µs, then after about 10 µs the two ends snap together, forming the ring seen in Fig. 4(d).

The initial spike in P^{mag} and rapid decrease in E^{ani} correspond to the initial relaxation of all moments towards their respective anisotropy axes. After this relaxation there are virtually no Gilbert losses and E^{ani} is nearly constant, i.e., even though the LLG equation is used throughout, the moment rotation remains locked to the mechanical rotation. This would have justified using the rigid dipole approximation, especially since the random, initial moment configuration is implausible in an experiment.

For the first 3 µs there are steady rotational losses, while the translational losses are marked by spikes. The reason is that whenever two or more MNPs collide, the translational loss rate increases as the MNPs accelerate, then drops sharply while they settle in the combined minimum of the dipole and WCA potentials. E^{WCA} is seen to increase as more and more MNPs reach surface contact. The dissipated energy largely comes from the dipolar interactions, as seen by the consistent decrease of E^{dip}. The curves all remain nearly flat after 3 µs, except around $t = 10$ µs when the MNP chain snaps into a ring causing one more spike in P^{trans}. This illustrates how the relaxation of MNP systems occurs across many timescales.

This example simulation is in stark contrast to Fig. 3, as the losses from a few ns and onwards are exclusively viscous. Thus, for a more realistic initial state with relaxed moments, instead of heating the MNPs directly, the energy goes to exciting the surrounding fluid. In reality, thermal fluctuations will transfer kinetic energy from the fluid back into the particles, so the whole system reaches a uniform temperature eventually, but at no point will the MNP cores be hotter than the surrounding fluid.

3. Hysteresis during collision

As a final use case, in Fig. 5 we consider two MNPs colliding under a 1-MHz sinusoidal driving field. We have $B^{\text{ani}} = 50$ mT and found by repeated simulations that for B^{ext} between 25 and 50 mT, a sudden change in behavior occurs as the MNPs get nearer. In Fig. 5 we chose $B^{\text{ext}} = 40$ mT to illustrate this.

The first part of the curve is similar to Fig. 3 even though there are now two interacting MNPs. This is because at the initial distance of $d = 50$ nm the field from one MNP on the other is at most $2\mu_0\mu/(4\pi d^3) = 2.7$ mT [cf. Eq. (1)], i.e., their interaction is much weaker than the driving field, so they respond nearly as if isolated. From Fig. 5(b) we note spikes in E^{dip} during each moment reversal, which are small
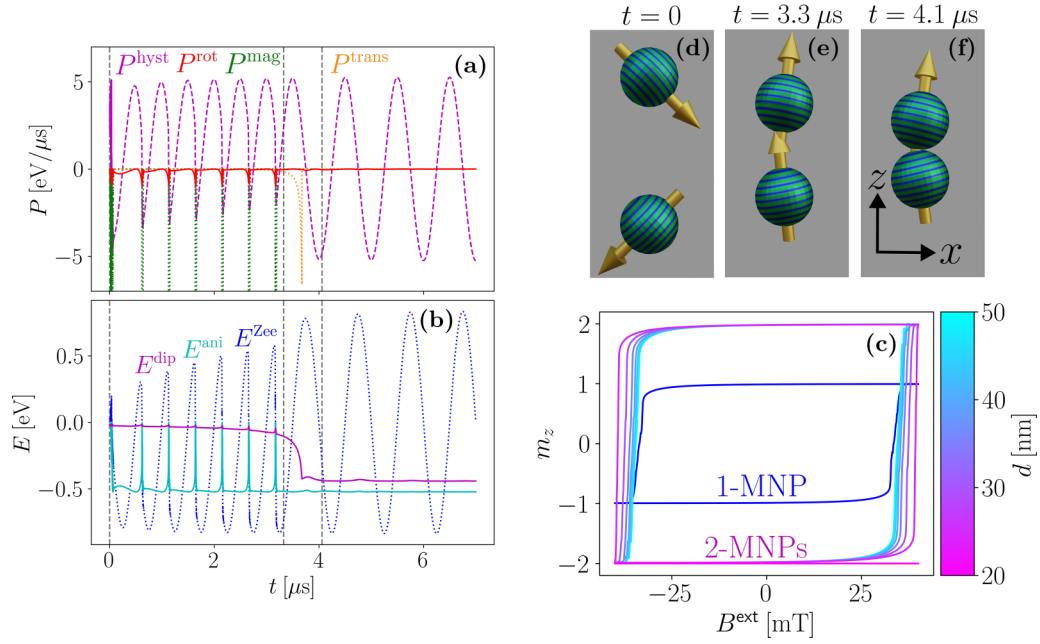
FIG. 5. 2MNPs colliding in an alternating field. Same parameters as in Fig. 3. The initial state is seen in (d) with coordinate axes in (f). The plots are identical for inertial and overdamped simulations. (a), (b) Evolution of power and energy contributions in time. Vertical, gray lines correspond to the configuration pictures in (d)–(f). The anisotropy axes are perpendicular to the blue circles, the arrows represent magnetic moments, and the sizes and distances are to scale. (c) Hysteresis curves simulated with the MNPs free to rotate, but fixed at a center-to-center distance of d. m_z is the z component of system moment relative to the moment per particle. A single-particle hysteresis curve is shown for comparison. The simulation is animated in the Supplemental Material [57].

compared to the E^{ani} spikes. The reason is that the MNPs flip simultaneously, so their moments remain nearly aligned, thus limiting the variation in E^{dip}. The E^{dip} spikes grow with decreasing distance, indicating increased losses from the dipolar coupling.

In Fig. 5(c), we confirm that the hysteresis losses grow as the MNPs approach each other, by computing hysteresis curves with positions fixed. The height is locked by the total moment, but the width increases with decreasing d. That is the dipole interaction increases the coercive field, making the two-MNP system a harder magnet. Indeed, when the coercive field exceeds B^{ext}, the loop closes entirely and the MNP behavior qualitatively changes.

In the second part of Figs. 5(a) and 5(b) moment reversal ceases as the MNPs collide. The collision is signified by a drop in E^{dip}, due to the rapidly diminishing distance [cf. Figs. 5(e) and 5(f)], and a spike in translational dissipation, due to the velocity changes around impact. This same decrease in distance means stronger dipole coupling, which is why moment reversal ceases. Because both velocity and dipole field strength scale nonlinearly with distance, most of the coercivity change occurs in the last fraction of the collision. Therefore, the moment locking nearly coincides with the impact for a broad parameter range. After some final rotational relaxation, the MNPs cease all motion. P^{hyst} and E^{Zee} still oscillate in tune with the driving field, but they are symmetric around 0, so there is no net energy transfer nor any dissipation.

In summary, the dipole coupling increases the coercive field as the MNPs draw nearer, resulting in a sudden change of the moment dynamics which ends all magnetic losses. The

MNPs then collide and stop moving entirely. We note that while some of this was elucidated by simulating multiple hysteresis curves, the entire story can be inferred from Fig. 5(a) alone, which is a single simulation that also shows the relative importance of magnetic and viscous losses, and the point of impact. Also, as demonstrated in Fig. 4, the presented plotting techniques scale well to many-particle systems.

VI. MODEL GENERALIZATIONS

So far in this paper, we restricted all analysis to the model we implemented and tested numerically. However, both the formal procedure for deriving our model and the formal results on transfer rates for conserved quantities readily generalize to a broader setting.

A. Spherical particles

For single-domain MNPs of multiple sizes and materials, the only difference is a subscript on α_i, γ_i', I_i, $\mathfrak{m}_i$, $\zeta_i^{\text{t(r)}}$, and μ_i to signify that these parameters vary between particles. A coating layer can be included by using the hydrodynamic radius for the damping coefficients in Eq. (17), and for surface forces like Eq. (45), but core radius elsewhere as in Ref. [32].

For nanomagnets with nonuniform magnetization, the notion of a single-particle moment is at best an approximation, so a rigorous treatment would require considerable further analysis.

Depending on the crystal symmetries of the magnetic core, a large number of higher-order magnetocrystalline anisotropy terms are possible, enabling any number of easy or hard axes [62,64,65]. For uniformly magnetized objects, shape

anisotropy only modifies the K tensor from Sec. II A 2, yielding uniaxial or triaxial anisotropy [25]. These additional anisotropies only change the functional form of $\mathbf{B}^{\mathrm{ani}}$, not how it enters the remaining equations.

B. Nonspherical particles

For nonspherical particles in liquid suspension, viscous drag becomes a tensor quantity. In general, at low Reynolds number in a stationary fluid, the viscous force and torque on an isolated particle are of the form [74,75]

$$\begin{pmatrix} \mathbf{F}_i^{\mathrm{visc}} \\ \boldsymbol{\tau}_i^{\mathrm{visc}} \end{pmatrix} = -Z \begin{pmatrix} \mathbf{v}_i \\ \boldsymbol{\omega}_i \end{pmatrix}, \ Z = \begin{pmatrix} Z^{\mathrm{tt}} & Z^{\mathrm{tr}} \\ Z^{\mathrm{rt}} & Z^{\mathrm{rr}} \end{pmatrix}, \tag{46}$$

where Z is a symmetric 6×6 matrix and $Z^{\mathrm{t(r),t(r)}}$ are 3×3 matrices. One can then straightforwardly generalize the derivation in Appendix D (see Supplemental Material [106]). The result is

$$\dot{E} = \sum_i \left(P_i^{\mathrm{hyst}} + P_i^{\mathrm{mag}} + P_i^{\mathrm{visc}} \right), \tag{47}$$

where P_i^{hyst}, P_i^{mag} are still given by Eqs. (37) and (38) while, using $\mathbf{f}_i^{\mathrm{th}} = (\mathbf{F}_i^{\mathrm{th}}, \boldsymbol{\tau}_i^{\mathrm{th}})$ and $\mathbf{V}_i = (\mathbf{v}_i, \boldsymbol{\omega}_i)$,

$$P_i^{\mathrm{visc}} = -\mathbf{V}_i \cdot Z\mathbf{V}_i + \mathbf{f}_i^{\mathrm{th}} \cdot \mathbf{V}_i.$$

P_i^{visc} is consistent with Refs. [84] and [[85], Sec. 2.2]. Similarly, the transfer of linear and angular momentum generalize to (see Supplemental Material [106])

$$\dot{\mathbf{p}} = \sum_i \left(\mathbf{F}_i^{\mathrm{visc}} + \mathbf{F}_i^{\mathrm{th}} \right), \tag{48}$$

$$\dot{\mathbf{J}} = \sum_i \left(\boldsymbol{\mu}_i \times \mathbf{B}^{\mathrm{ext}} + \boldsymbol{\tau}_i^{\mathrm{visc}} + \boldsymbol{\tau}_i^{\mathrm{th}} + \mathbf{r}_i \times \left[\mathbf{F}_i^{\mathrm{visc}} + \mathbf{F}_i^{\mathrm{th}} \right] \right). \tag{49}$$

Note that because of the coupling between the drag on different components of $\mathbf{V}$, there are also statistical correlations between components of the thermal fluctuations [107]. Therefore, instead of Eqs. (21) and (22) we have

$$\left\langle f_\alpha^{\mathrm{th}}(t) f_\beta^{\mathrm{th}}(t') \right\rangle = 2k_B T Z_{\alpha\beta} \delta(t - t'). \tag{50}$$

Another effect of nonspherical particles is that magnetic fields from the MNPs and the interaction energy E_{ij}^{int} are close to dipolar only at long range [108]. However, Appendixes C and D never use the dipole approximation, so the derivations are still valid. That is, Eq. (C2) becomes an integral equation for nonspherical magnets [108], but the transfer equations (47)–(49) are unchanged.

C. Additional interactions

Aside from magnetic interactions, MNPs in liquid suspension are subject to various surface-to-surface interactions, depending on the details of surface coating and fluid medium [109–112]. For example, when modeling MNP aggregation, a bare minimum is a model of steric repulsion to prevent MNP overlap, but simulations have also included ligand bonding [33,37], as well as electrostatic [113] and van der Waals forces [32] among others. All these can be modeled by interaction potentials, which depend only on the relative positions and orientations of MNP pairs. In general, interaction potentials can be appended to the system energy (7). Then one may

repeat the procedure in Sec. II to derive the resulting conservative forces and torques.

Finally, we consider the greatest simplifying assumption in this work, namely, the neglect of hydrodynamic interactions between MNPs. With multiple particles in liquid suspension, the velocity distribution of the fluid depends on the position and motion of every suspended particle. This leads to a long-range, many-body interaction [85,114], which fundamentally changes the mechanical equations of motion. One can make the problem computationally tractable by the methods and simplifications of Stokesian dynamics [115–117], which have been applied to MNP suspensions both with [35] and without [118,119] thermal fluctuations. Alternatively, one can use various approximations to the two-sphere problem to derive pair interactions. We refer to Ref. [120] for a historical overview, Ref. [121] for lubrication theory (lowest order, short-range model), and Refs. [122–124] for a more complete analysis. Regardless of the level of approximation, the mathematical form of viscous drag is altered, so Eqs. (47)–(49) are not directly applicable.

In summary, the transfer equations (47)–(49) hold for any collection of arbitrarily shaped but uniformly magnetized nanoparticles, when neglecting electrodynamic and hydrodynamic interactions and assuming that the driving field $\mathbf{B}^{\mathrm{ext}}$ is uniform across a particle.

VII. CONCLUSIONS

We derived a general model of the energy, linear, and angular momentum for a collection of interacting magnetic nanoparticles in an external magnetic field. Starting from these conserved quantities, we used a formal, easily generalizable procedure for deriving the equations of motion in liquid suspension, at finite temperature. The result is a set of Langevin equations which couple the LLG equation for moment rotation with the mechanical translation and rotation of the particles.

Within this model we derived expressions for the transfer of energy and momenta between system and environment, which we validated numerically by time-step integration. This both demonstrates self-consistency of the model, and that we can numerically analyze the transfer rates at finite temperature, despite the technical difficulties of integrating stochastic processes.

We note that a number of established models and analyses can be derived as special cases or approximations to our results: for example, the RDA, the hysteresis curve area as a measure of energy dissipation or the recent analyses by Leliaert *et al.* [49] and Helbig *et al.* [45] on energy transfer.

In addition to model development and verification, tracking the transfer of conserved quantities gives new insight on the physical system. Using the formulas in this paper, one can calculate the instantaneous power at each MNP and decompose into different transfer channels. In particular, power absorbed from the driving field, magnetic losses from Gilbert damping, and viscous losses to the fluid, both translational and rotational. Whether the losses are magnetic or viscous determines whether heating occurs inside the particles or in the surrounding fluid. By simulating zero-temperature hysteresis and aggregation in 1-, 2-, and 10-particle systems we

demonstrate how tracking power and energy contributions gives new ways to visualize and interpret MNP dynamics, which are applicable to many-particle simulations.

Our results give a different perspective on known steady-state phenomena, useful tools for analyzing MNPs as mechanical actuators and hyperthermia agents, and may facilitate new studies on the transient and driven dynamics of nanomagnets.

APPENDIX A: REWRITING THE LLG EQUATION

Equation 23 defines $\dot{\mathbf{m}}$ recursively. Taking the recursion one step further, it may be rewritten

$$\dot{\mathbf{m}}_i = -\gamma \mathbf{m}_i \times \mathbf{B}_i^{\text{eff}} + \alpha_i \mathbf{m}_i \times \left[-\gamma \mathbf{m}_i \times \mathbf{B}_i^{\text{eff}} + \alpha_i \mathbf{m}_i \times \dot{\mathbf{m}}_i \right].$$

We recall that $\mathbf{m}$ has constant magnitude $m^2 = 1$. Differentiating yields $\mathbf{m} \cdot \dot{\mathbf{m}} = 0$, i.e., $\dot{\mathbf{m}}$ is perpendicular to $\mathbf{m}$. It follows that $\mathbf{m} \times [\mathbf{m} \times \dot{\mathbf{m}}] = -m^2 \dot{\mathbf{m}} = -\dot{\mathbf{m}}$. Thus, we can isolate $\dot{\mathbf{m}}$, which yields Eq. (25).

APPENDIX B: MECHANICAL EQUATIONS OF MOTION

For translation, simply add the damping and thermal force from Sec. II D to the right-hand side of Eq. (11) to get (27). For rotation it follows from (14) that

$$\dot{\mathbf{L}}_i = \dot{\mathbf{L}}_i\big|_{\alpha=0} + \dot{\mathbf{S}}_i\big|_{\alpha=0} - \dot{\mathbf{S}}_i.$$

Writing out the viscous and damping torque, then using the angular momentum definitions [Eq. (4)]

$$I\dot{\boldsymbol{\omega}}_i = I\dot{\boldsymbol{\omega}}_i\bigg|_{\zeta^r=\alpha=0} + \frac{\mu}{\gamma}\left(\dot{\mathbf{m}}_i - \dot{\mathbf{m}}_i\big|_{\alpha=0}\right) - \zeta^r \boldsymbol{\omega}_i + \boldsymbol{\tau}_i^{\text{th}}.$$

Inserting the equations without damping, Eqs. (9) and (10), yields Eq. (26).

APPENDIX C: CONSERVATION LAWS IN MAGNETOSTATICS

In the framework of electrodynamics, linear and angular momentum conservation can be shown formally for any finite distribution of charges and currents [80]. Here, we use a simpler version of the same argument for a finite current distribution in magnetostatics. Note that the current distribution may change in time, as long as forces, torques, and electromagnetic fields are calculated as if the instantaneous current distribution was steady.

Maxwells laws take the form

$$\nabla \cdot \mathbf{B} = 0, \ \nabla \times \mathbf{B} = \mu_0 \mathbf{J}_e, \ \mathbf{E} = 0,$$

where $\mathbf{J}_e$ is electrical current density. From the Lorentz force law, the force density is

$$\mathbf{f} = \mathbf{J}_e \times \mathbf{B} = \frac{1}{\mu_0}(\nabla \times \mathbf{B}) \times \mathbf{B} = \frac{1}{\mu_0}\left[(\mathbf{B} \cdot \nabla)\mathbf{B} - \frac{1}{2}\nabla B^2\right].$$

In component form, with $\partial_\alpha = \frac{\partial}{\partial r_\alpha}$, this may be written

$$f_\alpha = \sum_\beta \partial_\beta T_{\beta\alpha}, \quad T_{\beta\alpha} = \frac{1}{\mu_0}\left[B_\beta B_\alpha - \frac{1}{2}\delta_{\beta\alpha}B^2\right]. \quad \text{(C1)}$$

The tensor T is Maxwells stress tensor in the absence of $\mathbf{E}$ fields. The momentum density in the EM fields is $\epsilon_0 \mathbf{E} \times \mathbf{B} =$

0, hence, the rate of change of momentum is given by $\frac{\mathrm{d}}{\mathrm{d}t}p_\alpha = \int f_\alpha \, \mathrm{d}\mathbf{r}$. Integrating Eq. (C1) over all space and using Gauss theorem thus proves conservation of linear momentum.

Similarly, the components of the torque density are

$$\tau_\alpha = (\mathbf{r} \times \mathbf{f})_\alpha = \sum_\beta \partial_\beta M_{\beta\alpha}, \ M_{\beta\alpha} = \sum_{\gamma\delta} \epsilon_{\gamma\delta\alpha} x_\gamma T_{\beta\delta},$$

where $\epsilon_{\alpha\beta\gamma}$ is the Levi-Civita symbol. The change in angular momentum is given by $\frac{\mathrm{d}}{\mathrm{d}t}J_\alpha = \int \tau_\alpha \mathrm{d}\mathbf{r}$, which also gives zero by Gauss theorem.

In conclusion, in magnetostatics, linear and angular momentum are conserved without any field momentum. Since a magnetization distribution is equivalent to a collection of bound currents [60], the proof also applies to MNPs and other permanent magnets. In particular, for a collection of dipole magnets at zero temperature in vacuum it follows that

$$\frac{\mathrm{d}}{\mathrm{d}t}\mathbf{J}_{T=0}^{\text{vacuum}} = \sum_i \left(\mathbf{r}_i \times \mathbf{F}_i^{\text{dip}} + \boldsymbol{\mu}_i \times \mathbf{B}_i^{\text{dip}}\right) = 0. \quad \text{(C2)}$$

This can also be shown by inserting Eqs. (1) amd (13) for $\mathbf{B}^{\text{dip}}$, $\mathbf{F}^{\text{dip}}$, however, the present argument can be used to derive analogous identities for arbitrarily shaped magnets with higher-order multipole interactions.

APPENDIX D: TIME DERIVATIVE OF SYSTEM ENERGY

The system energy E is a function of the independent variables $\mathbf{m}_i, \mathbf{u}_i, \boldsymbol{\omega}_i, \mathbf{r}_i, \mathbf{v}_i, t$, so the time derivative is

$$\frac{\mathrm{d}}{\mathrm{d}t}E = \sum_i \left[\frac{\partial E}{\partial \mathbf{m}_i} \cdot \dot{\mathbf{m}}_i + \frac{\partial E}{\partial \mathbf{u}_i} \cdot \dot{\mathbf{u}}_i + \frac{\partial E}{\partial \boldsymbol{\omega}_i} \cdot \dot{\boldsymbol{\omega}}_i \right.$$
$$\left. + \frac{\partial E}{\partial \mathbf{r}_i} \cdot \mathbf{v}_i + \frac{\partial E}{\partial \mathbf{v}_i} \cdot \dot{\mathbf{v}}_i\right] + \frac{\partial E}{\partial t}. \quad \text{(D1)}$$

Here we assume the Stratonovich interpretation, which means the ordinary rules of calculus apply despite the stochastic terms [101,102]. In Sec. V B, we verify numerically that the Stratonovich interpretation is correct in the overdamped case.

We consider a single term and suppress the i subscript to avoid notational clutter. Let $\dot{\mathbf{m}}_0, \dot{\boldsymbol{\omega}}_0, \dot{\mathbf{p}}_0 = \mathfrak{m}\dot{\mathbf{v}}_0$ denote the derivatives in absence of damping [Eqs. (9)–(11)]. The derivatives with damping are given in Eqs. (23), (26), and (27) and $\dot{\mathbf{u}} = \boldsymbol{\omega} \times \mathbf{u}$ applies in both cases. For reference we recall the general vector identity

$$\mathbf{a} \cdot (\mathbf{b} \times \mathbf{c}) = \mathbf{b} \cdot (\mathbf{c} \times \mathbf{a}) = \mathbf{c} \cdot (\mathbf{a} \times \mathbf{b}).$$

The only explicit time dependence is in the external field, so

$$\frac{\partial E}{\partial t} = -\mu \mathbf{m} \cdot \dot{\mathbf{B}}^{\text{ext}}. \quad \text{(D2)}$$

By definition $\partial_{\mathbf{r}}E = -\dot{\mathbf{p}}_0$, hence,

$$\frac{\partial E}{\partial \mathbf{r}} \cdot \mathbf{v} = -\dot{\mathbf{p}}_0 \cdot \mathbf{v} = -(\mathfrak{m}\dot{\mathbf{v}} + \zeta^t \mathbf{v} - \mathbf{F}^{\text{th}}) \cdot \mathbf{v}$$
$$= -\mathbf{p} \cdot \dot{\mathbf{v}} - \zeta^t v^2 + \mathbf{F}^{\text{th}} \cdot \mathbf{v}.$$

Using Eq. (7), $\partial_{\mathbf{v}}E = \mathbf{p}$, thus,

$$\frac{\partial E}{\partial \mathbf{r}} \cdot \mathbf{v} + \frac{\partial E}{\partial \mathbf{v}} \cdot \dot{\mathbf{v}} = -\zeta^t v^2 + \mathbf{F}^{\text{th}} \cdot \mathbf{v}. \quad \text{(D3)}$$

Equation (D3) is the final result for the translational degrees of freedom.

For mechanical rotation we find, using Eqs. (8) and (28) and $\mathbf{L}_0 = I\boldsymbol{\omega}_0$, that

$$\frac{\partial E}{\partial \mathbf{u}} \cdot \dot{\mathbf{u}} = \frac{\partial E}{\partial \mathbf{u}} \cdot (\boldsymbol{\omega} \times \mathbf{u}) = -\boldsymbol{\omega} \cdot \left(\frac{\partial E}{\partial \mathbf{u}} \times \mathbf{u} \right) = -I\boldsymbol{\omega} \cdot \dot{\boldsymbol{\omega}}_0$$

while

$$\frac{\partial E}{\partial \boldsymbol{\omega}} \cdot \dot{\boldsymbol{\omega}} = I\boldsymbol{\omega} \cdot \dot{\boldsymbol{\omega}}.$$

Inserting Eqs. (10) and (26) yields

$$\frac{\partial E}{\partial \mathbf{u}} \cdot \dot{\mathbf{u}} + \frac{\partial E}{\partial \boldsymbol{\omega}} \cdot \dot{\boldsymbol{\omega}} = I\boldsymbol{\omega} \cdot (\dot{\boldsymbol{\omega}} - \dot{\boldsymbol{\omega}}_0)$$

$$= \frac{\mu}{\gamma}\boldsymbol{\omega} \cdot (\dot{\mathbf{m}} - \dot{\mathbf{m}}_0) - \zeta^{\mathrm{r}}\omega^2 + \boldsymbol{\omega} \cdot \boldsymbol{\tau}^{\mathrm{th}}.$$
$$\text{(D4)}$$

For magnetic rotation, we find analogously that

$$\frac{\partial E}{\partial \mathbf{m}} \cdot \dot{\mathbf{m}} = \frac{\partial E}{\partial \mathbf{m}} \cdot (\boldsymbol{\Omega} \times \mathbf{m}) = -\boldsymbol{\Omega} \cdot \dot{\mathbf{S}}_0 = \frac{\mu}{\gamma}\boldsymbol{\Omega} \cdot \dot{\mathbf{m}}_0,$$

where $\boldsymbol{\Omega}$ is defined in Eq. (29) and $\dot{\mathbf{S}}_0 = \partial_{\mathbf{m}}E \times \mathbf{m}_0$. We note that $\boldsymbol{\Omega} \cdot \dot{\mathbf{m}} = \boldsymbol{\Omega} \cdot (\boldsymbol{\Omega} \times \mathbf{m}) = 0$, so

$$\frac{\partial E}{\partial \mathbf{m}} \cdot \dot{\mathbf{m}} = \frac{\mu}{\gamma}\boldsymbol{\Omega} \cdot (\dot{\mathbf{m}}_0 - \dot{\mathbf{m}}). \quad \text{(D5)}$$

Now, adding Eqs. (D4) and (D5) we get

$$\frac{\partial E}{\partial \mathbf{u}} \cdot \dot{\mathbf{u}} + \frac{\partial E}{\partial \boldsymbol{\omega}} \cdot \dot{\boldsymbol{\omega}} + \frac{\partial E}{\partial \mathbf{m}} \cdot \dot{\mathbf{m}}$$

$$= \frac{\mu}{\gamma}(\boldsymbol{\Omega} - \boldsymbol{\omega}) \cdot (\dot{\mathbf{m}}_0 - \dot{\mathbf{m}}) - \zeta^{\mathrm{r}}\omega^2 + \boldsymbol{\omega} \cdot \boldsymbol{\tau}^{\mathrm{th}}. \quad \text{(D6)}$$

It follows from Eqs. (9), (23), and (24) that

$$\dot{\mathbf{m}}_0 - \dot{\mathbf{m}} = \gamma \mathbf{m} \times \mathbf{B}^{\mathrm{th}} - \alpha \mathbf{m} \times (\boldsymbol{\Omega} \times \mathbf{m} - \gamma \mathbf{B}^{\mathrm{Bar}}).$$

Inserting the definition of the Barnett field, Eq. (16), this can be written

$$\dot{\mathbf{m}}_0 - \dot{\mathbf{m}} = \gamma \mathbf{m} \times [\mathbf{B}^{\mathrm{th}} - \alpha(\boldsymbol{\Omega} - \boldsymbol{\omega}) \times \mathbf{m}].$$

Hence,

$$\frac{\mu}{\gamma}(\boldsymbol{\Omega} - \boldsymbol{\omega}) \cdot (\dot{\mathbf{m}}_0 - \dot{\mathbf{m}})$$

$$= \mu[(\boldsymbol{\Omega} - \boldsymbol{\omega}) \times \mathbf{m}] \cdot \mathbf{B}^{\mathrm{th}} - \alpha\mu\gamma^{-1}([\boldsymbol{\Omega} - \boldsymbol{\omega}] \times \mathbf{m})^2.$$
$$\text{(D7)}$$

Inserting Eq. (D7) in (D6) then adding Eqs. (D2) and (D3) gives the energy transfer expressed in Eqs. (36)–(40).

We emphasize that no approximations were used, so within the model of Sec. II E the derived energy transfer is exact under the Stratonovich interpretation. The result is unchanged in the overdamped limit, i.e., when setting $\mathfrak{m} = I = 0$, and we never explicitly used the form of the dipole interactions, so the proof applies to any magnetostatic interactions.

We note that the same derivation applies to a single, isolated MNP, which indicates that the energy transfer described by the ith term of Eq. (36) occurs locally at and around the ith MNP. This is consistent with the nature of the damping mechanisms.

If we instead consider a single MNP embedded in an interacting system, then it is ambiguous how much of the shared dipole energy to assign it. For the sake of argument let interaction energies be distributed equally between each particle pair, so that $E_i^{\mathrm{int}} = -\frac{1}{2}\boldsymbol{\mu}_i \cdot \mathbf{B}_i^{\mathrm{dip}}$. Then the derivation is identical, except that the $\partial_t E$ term gives an extra power of the form $P_i^{\mathrm{int}} = -\frac{1}{2}\boldsymbol{\mu}_i \cdot \dot{\mathbf{B}}_i^{\mathrm{dip}}$, which is analogous to P_i^{hyst}. After all, the individual MNP cannot tell if a B-field contribution comes from outside the system like $\mathbf{B}^{\mathrm{ext}}$ or from the other MNPs. P_i^{int} fully accounts for the energy exchange between particles due to magnetic interactions, which is further evidence that viscous and Gilbert damping occur locally and only describe energy exchange with the environment.

APPENDIX E: NUMERICAL IMPLEMENTATION

For simulations in the overdamped limit, we use the time-stepping procedure:

Overdamped limit:
(i) Update $\mathbf{F}^{\mathrm{th}}$, $\boldsymbol{\tau}^{\mathrm{th}}$, $\mathbf{B}^{\mathrm{th}}$;
(ii) Compute $\mathbf{v}_i^n$, $\boldsymbol{\omega}_i^n$, $\boldsymbol{\Omega}_i^n$ [Eqs. (29), (43), (44)];
(iii) $(\mathbf{m}_i^n, \mathbf{u}_i^n, \mathbf{r}_i^n) \rightarrow (\mathbf{m}_i^{n+1/2}, \mathbf{u}_i^{n+1/2}, \mathbf{r}_i^{n+1/2})$;
(iv) Compute $\mathbf{v}_i^{n+1/2}$, $\boldsymbol{\omega}_i^{n+1/2}$, $\boldsymbol{\Omega}_i^{n+1/2}$;
(v) Compute $\dot{E}^{n+1/2}$ [Eq. (36)];
(vi) $E^{n+1} = E^n + \Delta t \dot{E}^{n+1/2}$;
(vii) $(\mathbf{m}_i^{n+1/2}, \mathbf{u}_i^{n+1/2}, \mathbf{r}_i^{n+1/2}) \rightarrow (\mathbf{m}_i^{n+1}, \mathbf{u}_i^{n+1}, \mathbf{r}_i^{n+1})$;
(viii) Repeat from top.

Here n is the time-step index, i.e., $t_n = n\Delta t$ so, for example, $E^n = E(t = n\Delta t)$. We use the Euler method for translations and the Euler-Rodriguez formula for rotations [99], i.e.,

$$\mathbf{m}_i^{n+1/2} = \mathrm{Rot}(\mathbf{m}_i^n, \Delta t \boldsymbol{\Omega}_i^n/2),$$

$$\mathbf{u}_i^{n+1/2} = \mathrm{Rot}(\mathbf{u}_i^n, \Delta t \boldsymbol{\omega}_i^n/2),$$

$$\mathbf{r}_i^{n+1/2} = \mathbf{r}_i^n + \tfrac{1}{2}\Delta t \mathbf{v}_i^n,$$

where

$$\mathrm{Rot}(\mathbf{u}, \boldsymbol{\theta}) = \mathbf{u}\cos\theta + (\hat{\boldsymbol{\theta}} \times \mathbf{u})\sin\theta + (\hat{\boldsymbol{\theta}} \cdot \mathbf{u})(1 - \cos\theta)\hat{\boldsymbol{\theta}}.$$

For the stochastic vectors, each component is drawn independently from a Gaussian distribution with zero mean and variances given in Eqs. (20)–(22). Since the algorithm uses discrete time $\delta(t - t') \rightarrow \frac{1}{\Delta t}\delta_{nn'}$, so for example F_x^{th}, F_y^{th}, and F_z^{th} all have a variance of $2k_B T \zeta^{\mathrm{t}}/\Delta t$. The meaning of $\delta_{nn'}$ is that $\mathbf{F}^{\mathrm{th}}$, $\boldsymbol{\tau}^{\mathrm{th}}$, $\mathbf{B}^{\mathrm{th}}$ should be redrawn at random every time step.

Note that when computing $\mathbf{v}$, $\boldsymbol{\omega}$, $\boldsymbol{\Omega}$ we compute all deterministic contributions to $\mathbf{F}$, $\boldsymbol{\tau}$, and $\mathbf{B}^{\mathrm{eff}}$ both at t_n and $t_{n+1/2}$, but the stochastic contributions are only changed at t_n. Since power is evaluated at $t_{n+1/2}$, this amounts to a midpoint integration of energy, also known as a Stratonovich integral. If $\dot{E}$ was instead evaluated at the same point in time where we update $\mathbf{F}^{\mathrm{th}}$, $\boldsymbol{\tau}^{\mathrm{th}}$, $\mathbf{B}^{\mathrm{th}}$ it would be an Itô integral, which entails artificial thermal drift in the energy, even at vanishingly small time step.

We also tested a combination of the Euler-Rodriguez formula and Heuns' method:

$$\tilde{\mathbf{m}}_i^{n+1/2} = \mathrm{Rot}\big(\mathbf{m}_i^n, \Delta t\, \boldsymbol{\Omega}_i^n/2\big),$$

$$\overline{\boldsymbol{\Omega}_i^n} = \frac{1}{2}\big(\boldsymbol{\Omega}_i^n + \boldsymbol{\Omega}\big[\tilde{\mathbf{m}}_i^{n+1/2}, \mathbf{u}_i^n, \mathbf{r}_i^n\big]\big),$$

$$\mathbf{m}_i^{n+1/2} = \mathrm{Rot}\big(\mathbf{m}_i^n, \Delta t\, \overline{\boldsymbol{\Omega}_i^n}/2\big).$$

That is, instead of using the angular velocity at t_n, we use the predicted moment $\tilde{\mathbf{m}}_i^{n+1/2}$ to estimate the average angular velocity $\overline{\boldsymbol{\Omega}_i^n}$ between t_n and $t_{n+1/2}$.

For calculations with inertia, we use the following procedure:

With inertia:

(i) Update $\mathbf{F}^{\mathrm{th}}$, $\boldsymbol{\tau}^{\mathrm{th}}$, $\mathbf{B}^{\mathrm{th}}$;

(ii) $(\mathbf{m}_i^n, \mathbf{u}_i^n, \mathbf{r}_i^n) \rightarrow (\mathbf{m}_i^{n+1/2}, \mathbf{u}_i^{n+1}, \mathbf{r}_i^{n+1})$;

(iii) Compute $\dot{\mathbf{v}}_i^{n+1}$, $\dot{\boldsymbol{\omega}}_i^n$, $\boldsymbol{\Omega}_i^{n+1/2}$ [Eqs. (26),(27),(29)];

(iv) $(\mathbf{v}_i^n, \boldsymbol{\omega}_i^n) \rightarrow (\mathbf{v}_i^{n+1}, \boldsymbol{\omega}_i^{n+1})$;

(v) Compute $\dot{\mathbf{J}}^{n+1/2}$ [Eq. (34)];

(vi) $\mathbf{m}_i^{n+1/2} \rightarrow \mathbf{m}_i^{n+1}$;

(vii) Repeat from top.

We use the Euler method for updating $\mathbf{v}$, $\boldsymbol{\omega}$, $\mathbf{r}$ and the Euler-Rodriguez formula for rotating $\mathbf{m}$, $\mathbf{u}$.

Our momentum integration is an end-point integration in terms of the mechanical variables and midpoint in terms of magnetic moment. This works because we only observed thermal drift in the magnetic angular momentum $\mathbf{S}$, not in the mechanical $\mathbf{L}$. We have not found a method for eliminating thermal drift in the energy integration, when both temperature and inertia are included.

[1] M. Zambach, M. Varón, M. Knaapila, Z. Ouyang, M. Beleggia, and C. Frandsen, High-susceptibility nanoparticles for micro-inductor core materials, arXiv:2308.13407.

[2] M. R. Almind, M. G. Vinum, S. T. Wismann, M. F. Hansen, S. B. Vendelbo, J. S. Engbæk, P. M. Mortensen, I. Chorkendorff, and C. Frandsen, ACS Appl. Nano Mater. **4**, 11537 (2021).

[3] S. R. Yassine, Z. Fatfat, G. H. Darwish, and P. Karam, Catal. Sci. Technol. **10**, 3890 (2020).

[4] R. Tietze, J. Zaloga, H. Unterweger, S. Lyer, R. P. Friedrich, C. Janko, M. Pöttler, S. Dürr, and C. Alexiou, Biochem. Biophys. Res. Commun. **468**, 463 (2015).

[5] Q. A. Pankhurst, J. Connolly, S. K. Jones, and J. Dobson, J. Phys. D: Appl. Phys. **36**, R167 (2003).

[6] Q. A. Pankhurst, N. T. K. Thanh, S. K. Jones, and J. Dobson, J. Phys. D: Appl. Phys. **42**, 224001 (2009).

[7] E. A. Périgo, G. Hemery, O. Sandre, D. Ortega, E. Garaio, F. Plazaola, and F. J. Teran, Appl. Phys. Rev. **2**, 041302 (2015).

[8] K. Wu, D. Su, J. Liu, R. Saha, and J.-P. Wang, Nanotechnology **30**, 502003 (2019).

[9] N. Panagiotopoulos, R. L. Duschka, M. Ahlborg, G. Bringout, C. Debbeler, M. Graeser, C. Kaethner, K. Lüdtke-Buzug, H. Medimagh, J. Stelzner, T. M. Buzug, J. Barkhausen, F. M. Vogt, and J. Haegele, Int. J. Nanomed. **10**, 3097 (2015).

[10] R. E. Rosensweig, J. Magn. Magn. Mater. **252**, 370 (2002).

[11] J. Carrey, B. Mehdaoui, and M. Respaud, J. Appl. Phys. **109**, 083921 (2011).

[12] E. Cazares-Cortes, S. Cabana, C. Boitard, E. Nehlig, N. Griffete, J. Fresnais, C. Wilhelm, A. Abou-Hassan, and C. Ménager, Adv. Drug Delivery Rev. **138**, 233 (2019).

[13] C. Haase and U. Nowak, Phys. Rev. B **85**, 045435 (2012).

[14] C. Muñoz-Menendez, D. Serantes, O. Chubykalo-Fesenko, S. Ruta, O. Hovorka, P. Nieves, K. L. Livesey, D. Baldomir, and R. Chantrell, Phys. Rev. B **102**, 214412 (2020).

[15] P. Torche, C. Munoz-Menendez, D. Serantes, D. Baldomir, K. L. Livesey, O. Chubykalo-Fesenko, S. Ruta, R. Chantrell, and O. Hovorka, Phys. Rev. B **101**, 224429 (2020).

[16] J. Ortega-Julia, D. Ortega, and J. Leliaert, Nanoscale **15**, 10342 (2023).

[17] A. Coene and J. Leliaert, Sensors **20**, 3882 (2020).

[18] D. F. Coral, P. Mendoza Zélis, M. Marciello, M. d. P. Morales, A. Craievich, F. H. Sánchez, and M. B. Fernández van Raap, Langmuir **32**, 1201 (2016).

[19] C. Guibert, V. Dupuis, V. Peyre, and J. Fresnais, J. Phys. Chem. C **119**, 28148 (2015).

[20] C. Naud, C. Thébault, M. Carrière, Y. Hou, R. Morel, F. Berger, B. Diény, and H. Joisten, Nanoscale Adv. **2**, 3632 (2020).

[21] Y. I. Golovin, S. L. Gribanovsky, D. Y. Golovin, N. L. Klyachko, A. G. Majouga, A. M. Master, M. Sokolsky, and A. V. Kabanov, J. Controlled Release **219**, 43 (2015).

[22] W. Coffey and Y. P. Kalmykov, *The Langevin Equation: With Applications to Stochastic Problems in Physics, Chemistry, and Electrical Engineering*, 4th ed., World Scientific Series in Contemporary Chemical Physics, Vol. 28 (World Scientific, Singapore, 2017).

[23] T. V. Lyutyy, E. S. Denisova, and A. V. Kvasnina, in *2017 IEEE 7th International Conference Nanomaterials: Application Properties (NAP)* (IEEE, Piscataway, NJ, 2017), pp. 02MFPM09–1–02MFPM09–4.

[24] T. V. Lyutyy, O. M. Hryshko, and A. A. Kovner, J. Magn. Magn. Mater. **446**, 87 (2018).

[25] H. Keshtgar, S. Streib, A. Kamra, Y. M. Blanter, and G. E. W. Bauer, Phys. Rev. B **95**, 134447 (2017).

[26] S. I. Denisov, T. V. Lyutyy, and A. T. Liutyi, J. Nano Electron. Phys. **12**, 06028 (2020).

[27] P. F. de Châtel, I. Nándori, J. Hakl, S. Mészáros, and K. Vad, J. Phys.: Condens. Matter **21**, 124202 (2009).

[28] C. Shasha and K. M. Krishnan, Adv. Mater. **33**, 1904131 (2021).

[29] J. Leliaert, J. Mulkers, J. De Clercq, A. Coene, M. Dvornik, and B. Van Waeyenberge, AIP Adv. **7**, 125010 (2017).

[30] S. Ruta, R. Chantrell, and O. Hovorka, Sci. Rep. **5**, 9090 (2015).

[31] M. Anand, J. Magn. Magn. Mater. **540**, 168461 (2021).

[32] F. L. Durhuus, L. H. Wandall, M. H. Boisen, M. Kure, M. Beleggia, and C. Frandsen, Nanoscale **13**, 1970 (2021).

[33] D. A. Rozhkov, E. S. Pyanzina, E. V. Novak, J. J. Cerdà, T. Sintes, M. Ronti, P. A. Sánchez, and S. S. Kantorovich, Mol. Simul. **44**, 507 (2018).

[34] N. R. Anderson, J. Davidson, D. R. Louie, D. Serantes, and K. L. Livesey, Nanomaterials **11**, 2870 (2021).

[35] A. Satoh, R. W. Chantrell, and G. N. Coverdale, J. Colloid Interface Sci. **209**, 44 (1999).

[36] J. S. Andreu, J. Camacho, and J. Faraudo, Soft Matter **7**, 2336 (2011).

[37] I. S. Novikau, P. A. Sánchez, and S. S. Kantorovich, J. Mol. Liq. **307**, 112902 (2020).

[38] X. Xue, J. Wang, and E. P. Furlani, ACS Appl. Mater. Interfaces **7**, 22515 (2015).

[39] D. V. Berkov, N. L. Gorn, R. Schmitz, and D. Stock, J. Phys.: Condens. Matter **18**, S2595 (2006).

[40] P. Kreissl, C. Holm, and R. Weeber, Soft Matter **17**, 174 (2021).

[41] N. Usov and O. Serebryakova, Sci. Rep. **10**, 13677 (2020).

[42] N. A. Usov and B. Y. Liubimov, J. Appl. Phys. **112**, 023901 (2012).

[43] K. D. Usadel and C. Usadel, J. Appl. Phys. **118**, 234303 (2015).

[44] K. D. Usadel, Phys. Rev. B **95**, 104430 (2017).

[45] S. Helbig, C. Abert, P. A. Sánchez, S. S. Kantorovich, and D. Suess, Phys. Rev. B **107**, 054416 (2023).

[46] T. V. Lyutyy and V. V. Reva, Phys. Rev. E **97**, 052611 (2018).

[47] D. Cabrera, A. Lak, T. Yoshida, M. E. Materia, D. Ortega, F. Ludwig, P. Guardia, A. Sathya, T. Pellegrino, and F. J. Teran, Nanoscale **9**, 5094 (2017).

[48] M.-K. Kim, J. Sim, J.-H. Lee, M. Kim, and S.-K. Kim, Phys. Rev. Appl. **9**, 054037 (2018).

[49] J. Leliaert, J. Ortega-Julia, and D. Ortega, Nanoscale **13**, 14734 (2021).

[50] T. Gilbert, IEEE Trans. Magn. **40**, 3443 (2004).

[51] K. Kustura, V. Wachter, A. E. Rubio López, and C. C. Rusconi, Phys. Rev. B **105**, 174439 (2022).

[52] N. Usov and B. Y. Liubimov, J. Magn. Magn. Mater. **385**, 339 (2015).

[53] M. Umeda, H. Chudo, M. Imai, N. Sato, and E. Saitoh, Rev. Sci. Instrum. **94**, 063906 (2023).

[54] C. C. Rusconi, V. Pöchhacker, K. Kustura, J. I. Cirac, and O. Romero-Isart, Phys. Rev. Lett. **119**, 167202 (2017).

[55] R. Kubo, Rep. Prog. Phys. **29**, 255 (1966).

[56] E. M. Purcell, Am. J. Phys. **45**, 3 (1977).

[57] See Supplemental Material at http://link.aps.org/supplemental/10.1103/PhysRevB.109.054421 which contains five videos with animations of the simulations shown in Fig. 2a and Figs. 3–5. Specifically for Figs. 2a, 3a, 3c, 4a and 5a, a Blender video of the MNPs moving around is shown next to the plot, with a moving vertical line in the plot whose time coordinate is synchronised to the video.

[58] B. O. Community, *Blender: A 3D Modelling and Rendering Package*, (Blender Foundation, Stichting Blender Foundation, Amsterdam).

[59] B. F. Edwards, D. M. Riffe, J.-Y. Ji, and W. A. Booth, Am. J. Phys. **85**, 130 (2017).

[60] D. J. Griffiths, *Introduction to Electrodynamics*, 4th ed. (Pearson, Boston, 2013).

[61] D. J. Griffiths, Am. J. Phys. **60**, 979 (1992).

[62] S. Bedanta, O. Petracic, and W. Kleemann, *Handbook of Magnetic Materials* (Elsevier, Amsterdam, 2015), Vol. 23, pp. 1–83.

[63] L. D. Landau and E. M. Lifshitz, *Electrodynamics of Continuous Media*, Vol. 8 (Pergamon, Oxford, 1960).

[64] S. Chikazumi, S. Chikazumi, and C. D. Graham, *Physics of Ferromagnetism* (Oxford University Press, Oxford, 1997), Vol. 94.

[65] B. D. Cullity and C. D. Graham, *Introduction to Magnetic Materials* (Wiley, Piscataway, NJ, 2011).

[66] D. J. Grifftihs, *Introduction to Quantum Mechanics*, 2nd ed. (Pearson, Boston, 2005).

[67] P. B. Landecker, D. D. Villani, and K. W. Yung, Magn. Elect. Separation **10**, 29 (1970).

[68] S. J. Barnett, Science **42**, 163 (1915).

[69] S. I. Rubinow and J. B. Keller, J. Fluid Mech. **11**, 447 (1961).

[70] W. F. Brown, Phys. Rev. **130**, 1677 (1963).

[71] S. J. Blundell and K. M. Blundell, *Concepts in Thermal Physics* (Oxford University Press, Oxford, 2010).

[72] A. Kamenev, *Field Theory of Non-Equilibrium Systems* (Cambridge University Press, Cambridge, 2011).

[73] Y. Han, A. M. Alsayed, M. Nobili, J. Zhang, T. C. Lubensky, and A. G. Yodh, Science **314**, 626 (2006).

[74] J. Happel and H. Brenner, in *Low Reynolds Number Hydrodynamics*, edited by R. J. Moreau, Mechanics of Fluids and Transport Processes, Vol. 1 (Springer, Dordrecht, 1981).

[75] H. Brenner, J. Colloid Interface Sci. **23**, 407 (1967).

[76] D. Babson, S. P. Reynolds, R. Bjorkquist, and D. J. Griffiths, Am. J. Phys. **77**, 826 (2009).

[77] R. H. Romer, Am. J. Phys. **34**, 772 (1966).

[78] V. Hnizdo, Am. J. Phys. **60**, 242 (1992).

[79] M. G. Christiansen, N. Mirkhani, W. Hornslien, and S. Schuerle, J. Appl. Phys. **132**, 174304 (2022).

[80] J. D. Jackson, *Classical Electrodynamics*, 3rd ed. (American Association of Physics Teachers, College Park, MD, 1999).

[81] N. L. Sharma, Am. J. Phys. **56**, 420 (1988).

[82] S. Streib, N. Vidal-Silva, K. Shen, and G. E. W. Bauer, Phys. Rev. B **99**, 184442(R) (2019).

[83] H. T. Simensen, A. Kamra, R. E. Troncoso, and A. Brataas, Phys. Rev. B **101**, 020403(R) (2020).

[84] R. Hill and G. Power, Quarterly J. Mech. Appl. Math. **9**, 313 (1956).

[85] S. Kim and S. J. Karrila, *Microhydrodynamics: Principles and Selected Applications*, Butterworth-Heinemann Series in Chemical Engineering (Butterworth-Heinemann, Boston, 1991).

[86] S. Singamaneni, V. N. Bliznyuk, C. Binek, and E. Y. Tsymbal, J. Mater. Chem. **21**, 16819 (2011).

[87] A. Michels, *Magnetic Small-Angle Neutron Scattering: A Probe for Mesoscale Magnetism Analysis* (Oxford University Press, Oxford, 2021), Vol. 16.

[88] S. Disch, E. Wetterskog, R. P. Hermann, A. Wiedenmann, U. Vainio, G. Salazar-Alvarez, L. Bergström, and T. Brückel, New J. Phys. **14**, 013025 (2012).

[89] F. Bødker, S. Mørup, and S. Linderoth, Phys. Rev. Lett. **72**, 282 (1994).

[90] K. L. Pisane, S. Singh, and M. S. Seehra, Appl. Phys. Lett. **110**, 222409 (2017).

[91] S. M. Bhagat and P. Lubitz, Phys. Rev. B **10**, 179 (1974).

[92] K. Gilmore, Y. U. Idzerda, and M. D. Stiles, Phys. Rev. Lett. **99**, 027204 (2007).

[93] W. Bailey, P. Kabos, F. Mancoff, and S. Russek, IEEE Trans. Magn. **37**, 6 (2001).

[94] S. Klingler, H. Maier-Flaig, C. Dubs, O. Surzhenko, R. Gross, H. Huebl, S. T. B. Goennenwein, and M. Weiler, Appl. Phys. Lett. **110**, 092409 (2017).

[95] H. Löwen, J. Chem. Phys. **152**, 040901 (2020).

[96] J. M. Hermansen, F. L. Durhuus, C. Frandsen, M. Beleggia, C. R. H. Bahl, and R. Bjørk, Phys. Rev. Appl. **20**, 044036 (2023).

[97] N. A. Usov, R. A. Rytov, and V. A. Bautin, Beilstein Journal of Nanotechnology **10**, 2294 (2019).

[98] W. Coffey and Yu. P. Kalmykov, J. Magn. Magn. Mater. **164**, 133 (1996).

[99] H. Cheng and K. C. Gupta, J. Appl. Mech. **56**, 139 (1989).

[100] P. Young, Lecture notes in University of California, Santa Cruz (unpublished).

[101] C. W. Gardiner, *Handbook of Stochastic Methods: For Physics, Chemistry and the Natural Sciences*, Springer Series in Synergetics, No. 13 (Springer, Berlin, 2002).

[102] S. Särkkä and A. Solin, *Applied Stochastic Differential Equations*, 1st ed. (Cambridge University Press, Cambridge, 2019).

[103] B. K. Øksendal, *Stochastic Differential Equations: An Introduction with Applications*, 5th ed. (Springer, Berlin, 1998).

[104] G. Pesce, A. McDaniel, S. Hottovy, J. Wehr, and G. Volpe, Nat. Commun. **4**, 2733 (2013).

[105] D. V. Berkov and N. L. Gorn, J. Phys.: Condens. Matter **14**, L281 (2002).

[106] See Supplemental Material at http://link.aps.org/supplemental/10.1103/PhysRevB.109.054421 for a generalization of the Langevin dynamics model to nonspherical particles with arbitrary anisotropy energy. Within this generalized model, we rederive the formal results on transfer of energy, linear, and angular momentum. This largely amounts to a repetition of the spherical case with more complex notation.

[107] D. L. Ermak and J. A. McCammon, J. Chem. Phys. **69**, 1352 (1978).

[108] M. Beleggia, S. Tandon, Y. Zhu, and M. De Graef, J. Magn. Magn. Mater. **278**, 270 (2004).

[109] Y. Min, M. Akbulut, K. Kristiansen, Y. Golan, and J. Israelachvili, *Nanoscience And Technology: A Collection of Reviews from Nature Journals* (World Scientific, Singapore, 2010), pp. 38–49.

[110] K. J. M. Bishop, C. E. Wilmer, S. Soh, and B. A. Grzybowski, Small **5**, 1600 (2009).

[111] J. Israelachvili, *Intermolecular and Surface Forces*, 3rd ed. (Academic, New York, 2011).

[112] S. Mørup, M. F. Hansen, and C. Frandsen, Beilstein J. Nanotechnol. **1**, 182 (2010).

[113] E. W. Chuan Lim and R. Feng, J. Chem. Phys. **136**, 124109 (2012).

[114] B. Cichocki, B. U. Felderhof, K. Hinsen, E. Wajnryb, and J. Blawzdziewicz, J. Chem. Phys. **100**, 3780 (1994).

[115] L. Durlofsky, J. F. Brady, and G. Bossis, J. Fluid Mech. **180**, 21 (1987).

[116] A. J. Banchio and J. F. Brady, J. Chem. Phys. **118**, 10323 (2003).

[117] J. F. Brady and G. Bossis, Annu. Rev. Fluid Mech. **20**, 111 (1988).

[118] A. Satoh, R. W. Chantrell, G. N. Coverdale, and S.-i. Kamiyama, J. Colloid Interface Sci. **203**, 233 (1998).

[119] A. Sand, J. F. Stener, M. O. Toivakka, J. E. Carlson, and B. I. Pålsson, Min. Eng. **90**, 70 (2016).

[120] B. D. Goddard, R. D. Mills-Williams, and J. Sun, Phys. Fluids **32**, 062001 (2020).

[121] W. B. Russel, D. A. Saville, and W. R. Schowalter, *Colloidal Dispersions*, Cambridge Monographs on Mechanics and Applied Mathematics (Cambridge University Press, Cambridge, 1989).

[122] D. J. Jeffrey and Y. Onishi, J. Fluid Mech. **139**, 261 (1984).

[123] D. J. Jeffrey, Phys. Fluids **4**, 16 (1992).

[124] A. K. Townsend, Phys. Fluids, **35**, 127126 (2023).